Trivalent Cations Slow Electron Transfer to Macrocyclic Heterobimetallic Complexes

Joseph P. Karnes,[a] Amit Kumar,[a,b] Julie A. Hopkins Leseberg,[a,c] Victor W. Day,[a] and James D. Blakemore,[a]*

[a] Department of Chemistry, University of Kansas, 1567 Irving Hill Road, Lawrence, Kansas 66045, United States

[b] Current address: Heraeus Precious Metals, 15524 Carmenita Road, Santa Fe Springs, California 90670, United States

[c] Current address: Research & Technology, Chevron Phillips Chemical, Kingwood, Texas 77339, United States

KEYWORDS: Electrochemistry; redox chemistry; synthesis; lanthanides; kinetics.

ABSTRACT: Incorporation of secondary redox-inactive cations into heterobimetallic complexes is an attractive strategy for modulation of metal-centered redox chemistry, but quantification of the consequences of incorporating strongly Lewis acidic trivalent cations has received little attention. Here, a family of seven heterobimetallic complexes that pair a redox-active nickel center with La^{3+}, Y^{3+}, Lu^{3+}, Sr^{2+}, Ca^{2+}, K^{+}, and Na^{+} (in the form of their triflate salts) have been

prepared on a heteroditopic ligand platform to understand how chemical behavior varies across the comprehensive series. Structural data from X-ray diffraction analysis demonstrate that the positions adopted by the secondary cations in the crown-ether-like site of the ligand relative to nickel are dependent primarily on the secondary cations' ionic radii, and that the triflate counter-anions are bound to the cations in all cases. Electrochemical data, in concert with electron paramagnetic resonance (EPR) studies, show that nickel(II)/nickel(I) redox is modulated by the secondary metals; the heterogeneous electron transfer (ET) rate is diminished for the derivatives incorporating trivalent metals, an effect that is dependent on steric crowding about the nickel metal center and that was quantified here with a topographical free-volume analysis. As related analyses carried out here on previously reported systems bear out similar relationships that were not noted in prior work, we conclude that the placement and identity of both the secondary metal cations and their associated counter-anions can afford unique changes in the (electro)chemical behavior of heterobimetallic species.

MAIN TEXT

Introduction

Gaining control over the electron transfer behaviors of redox-active molecules and materials is among the chief design challenges faced by synthetic inorganic chemists. The requirement to control redox chemistry, or at least reliably influence it, impacts development of molecular catalysts,[1,2] study of small molecule activation,[3,4] and efforts to observe the chemical properties of molecules featuring elements in uncommon oxidation states.[5,6,7] In each of these cases, understanding how the environment (coordination, solvation, etc.) of a given redox-active metal

can be modified to result in desirable redox properties is critical. Significant efforts are underway in a variety of fields to molecularly engineer the key features of electron transfer, including reduction potentials and electron transfer rates.[4] This broad interest is no doubt attributable to the numerous advantages that can come from favoring desirable redox reactions while disfavoring others, including increased selectivity in catalysis, increased efficiency in ET-dependent energy conversion systems, and improved yields during interconversion of oxidation states.

Incorporation of electropositive metal cations into complexes containing redox-active metal centers is a proven strategy for accessing chemical behaviors that are distinctive from those displayed by the analogous monometallic precursor complexes. In this realm, divergent synthetic protocols are most attractive, enabling access to families of complexes built from monometallic precursors that feature one or more binding sites for incorporation of secondary metal cations. Study of such complexes has shown that chemical properties such as reduction potentials,[3,8,9,10] energies of electronic absorption transitions,[5] energies of bond vibrations,[10] catalytic abilities,[2,3] and even magnetic behaviors[11] can be systematically tuned based on the identity of the incorporated secondary metal cations. Recently, we have gathered evidence for the hypothesis that, in cases where bridging ligands are present between redox-active metals and the incorporated secondary electropositive metal cations, there is an induced diminishment of the donor power of the bridging ligands that depends on the identity of the secondary cation.[10] Other frameworks for understanding the origin of tuning effects have also been developed, including the concepts of cation-induced electric fields,[12,13] cation-driven structural deformations,[14] and size-dependent behaviors.[2] Regardless of the interpretation around their origins, the use of cations to modulate redox chemistry is currently attracting significant attention as this strategy appears quite broadly useful.

The electropositive metal cations that are commonly used for tuning purposes span a range of charges, sizes, and coordination numbers, and often include mono- and divalent cations such as K^+, Na^+, Ba^{2+}, and Ca^{2+}. Trivalent cations such as Sc^{3+} attract special attention, however, as the effects that they promote are typically more significant than those of mono- and divalent cations. Generally speaking, this observation is related to demonstrations that electropositive metal cations, in effect, function as Lewis acids in most applications where they are incorporated into complexes to modulate redox chemistry. To rationalize cation-driven tuning effects on a unified and rather intuitive scale, Brønsted-Lowry acidity data for metal aqua complexes are often used, as gathered together by Perrin in an important and comprehensive catalogue.[15] The scale on which metal cations can be compared uses the pK_a values of water bound to metal aqua complexes of the metal cations of interest to parameterize their effect(s) on multimetallic complexes. This approach to describing tunable behaviors in heterobimetallic complexes, and larger systems, has proven robust across solvent systems.[16,17] The robustness of the scale likely derives from the observation that the experimental pK_a values shift reliably based on charge density,[18] taking into account both charge and ionic radius.[19,20]

Since beginning our own work in the area of heterobimetallic chemistry, we have noted a trend in the field: the properties of complexes containing a redox-active metal and a trivalent metal cation serving as a tuning agent often display properties that are the most dramatically shifted in any comparison series (see Chart 1). Important foundational work from Agapie and co-workers showed that trivalent rare-earth cations could be used to induce greatly shifted reduction potentials in manganese and iron clusters.[3] We showed later than although Nd^{3+} and Y^{3+} could be used as desired for tuning of redox-active nickel complexes, although derivatives containing these cations showed solvent-dependent stabilities in contrast to analogues incorporating mono-

or divalent secondary cations.[5] Nam and Fukuzumi have used Sc^{3+} to promote reactivity of oxygen-derived species, although the heterobimetallic species in those cases were assembled *in situ* to form the activated system.[4] A unifying theme of all these reports is that the high effective Lewis acidity of the trivalent cations appears to grant them a privileged position as drivers of significant and potentially useful changes in the chemical properties of redox-active metal complexes.

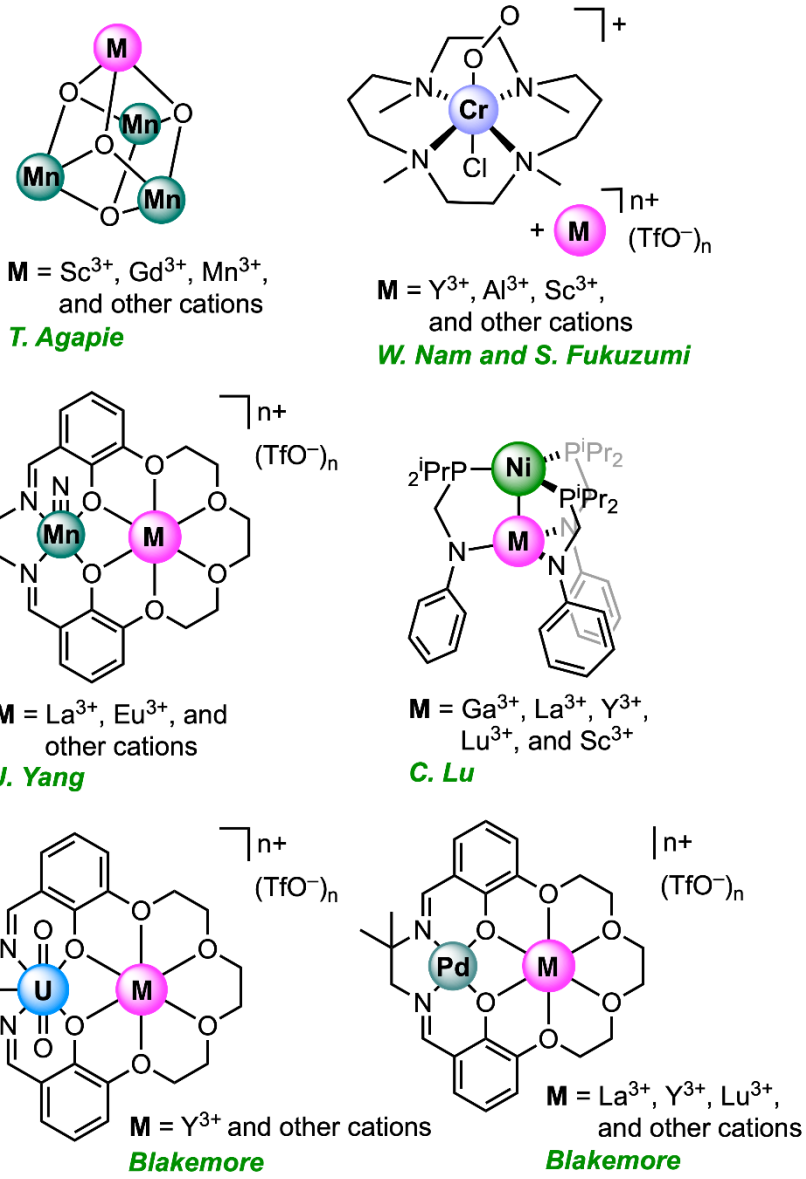

Chart 1. Examples of tunable heterobimetallic complexes containing trivalent secondary cations.

However, we have noted after reviewing the literature in this realm that few studies have examined the electron transfer kinetics of heterobimetallic complexes and how these kinetics may depend on the identity of the incorporated secondary metal cations. On the one hand, ET kinetics are critical in redox-induced turnover and the time-dependent yield of reduced/oxidized

products, impacting efficiency and selectivity considerations in inorganic/organometallic systems. On the other hand, numerous studies have examined the tuning of thermodynamic reduction potentials by incorporation of secondary, Lewis acidic metal cations into heterobimetallic complexes while neglecting the interrelated kinetic considerations. We anticipated that investigation of the tuning of ET kinetics by secondary metal cations would be enhanced, however, by comprehensive structural studies on the redox-active complexes chosen for investigation. In particular, we anticipated that study of a family of derivatives featuring mono-, di-, and trivalent secondary cations would be attractive, because the consequences of incorporating the important trivalent cations could be compared to those incorporating mono- and divalent cations in a systematic fashion.

Here, we now report the synthesis, isolation, and study of a collection of heterobimetallic nickel complexes built upon a Reinhoudt-type ligand framework that enable quantification of the influence of secondary metal cations on nickel(II)/nickel(I) redox chemistry. Incorporation of a broad range of metal cations (La^{3+}, Y^{3+}, Lu^{3+}, Sr^{2+}, Ca^{2+}, K^{+}, and Na^{+}) was carried out, and single-crystal X-ray diffraction data confirmed assembly of homologous [$Ni^{II}(\mu_2\text{-}O_{phenoxide})M^{n+}$] cores in all cases except that of the derivative featuring Y^{3+} (which resisted crystallization), providing a comprehensive series of complexes upon which to base an investigation of the role of the secondary metal cations in influencing the properties of the heterobimetallic species. The X-ray diffraction studies reveal that the position adopted by the secondary metal cations is dependent on their ionic radii, and that the triflate counter-anions associated with the secondary cations are bound inner-sphere in all cases, resulting in steric crowding about the redox-active nickel centers. This steric crowding impacts the heterogeneous electron transfer kinetics associated with nickel(II)/nickel(I) redox cycling, an effect that was quantified through a topographical buried-

volume analysis. As these observations suggest that trivalent cations and their counter-anions can directly impact tunable behaviors, this report identifies key structural design elements that can be used to influence the kinetics of electron transfer behavior in multimetallic systems.

Results

Synthesis and Characterization. Our group prefers to use a divergent synthetic strategy for the preparation of heterobimetallic complexes, and we have found that preparation of suitable monometallic precursor complexes can enable rapid access to derivatives featuring incorporated secondary metal cations. Here, we turned to a monometallic nickel(II) complex, denoted **[Ni]**, that was previously synthesized by Reinhoudt and co-workers.[21,22] **[Ni]** features a Schiff-base binding site for nickel as well as an appended crown-ether-like site for binding secondary cations (see Scheme 1). The ligand supporting the monometallic complex is quite useful (denoted here as $\mathbf{L}_{\mathbf{salmen}}$), as it is based on a 1,1-dimethyl-1,2-ethylenediamine-containing backbone that favors macrocyclization via the Thorpe-Ingold effect.[23] The favorability of the macrocyclization reaction enables isolation of **[Ni]** and subsequent use of this precursor for the divergent metalation that can yield the heterobimetallic complexes developed for our study. We note here that this approach differs from a prior study[13] that utilized convergent metalation to produce heterobimetallic complexes of nickel with mono- and divalent secondary metal cations; in that study, the utilization of simpler ethylenediamine as the ligand backbone appears to preclude study of adducts with trivalent cations. We prepared **[Ni]** as described by Reinhoudt and co-workers; the ^{1}H NMR spectrum of our isolated material matched well with results obtained in the prior work (see Figure S1).[21]

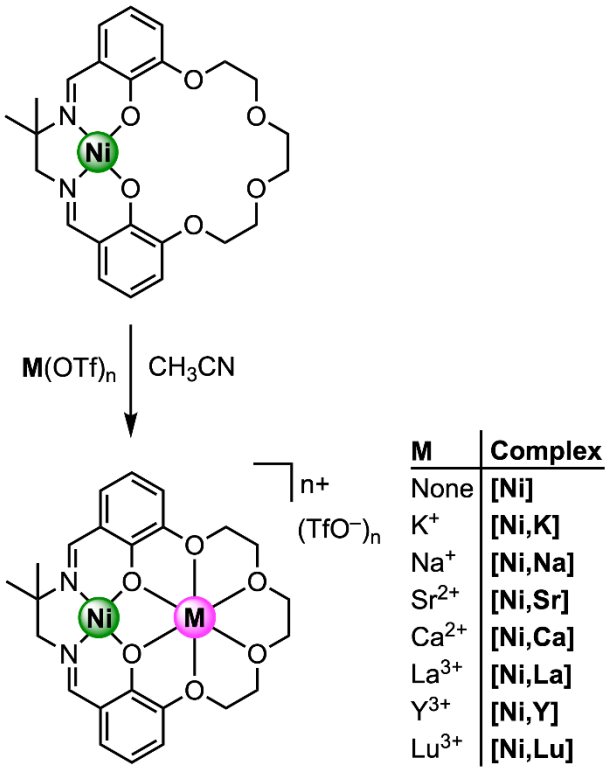

Scheme 1. Divergent synthetic strategy for heterobimetallic nickel complexes

With **[Ni]** in hand, heterobimetallic complexes of the form **[Ni,M]** could be prepared by reaction of the monometallic starting material with the corresponding metal triflate salts. Specifically, 1 equiv. of metal triflate salt was reacted with **[Ni]** to obtain 1:1 bimetallic complexes in high yields in all cases (95-98%; see Experimental Section). As in our previous work, we used the pK_a values of the metal-aqua complexes of the incorporated metal cations to describe their effective Lewis acidities; our work here spans from the weakly acidic K^+ (pK_a = 16.0) to strongly acidic Lu^{3+} (7.9).[15] ^{1}H, ^{13}C{^{1}H}, and ^{19}F NMR studies (see Figures S5-S39), as well as elemental analyses of all the isolated complexes were performed successfully, validating the clean formation of the targeted complexes. As we found in prior work with palladium(II)

complexes based on $\mathbf{L_{salmen}}$,[9] the downfield resonances corresponding to the imine protons of each complex are particularly diagnostic of coordination of the redox-inactive metal cations; strong downfield shifts are associated with the derivatives containing the more strongly Lewis acidic cations (see Figure S35 which shows the case of **[Ni,Lu]**). Additionally, no evidence was obtained for scrambling of the metal cations between the two sites of $\mathbf{L_{salmen}}$; this ligand can be concluded to effectively support orthogonal metalation.

Single-crystal X-ray Diffraction Analysis. XRD analysis of the heterobimetallic complexes confirmed assembly of the desired $[Ni^{II}(\mu_2\text{-}O_{phenoxide})M^{n+}]$ cores in each case (see Figure 1). See Table 1 for the metrical data obtained from the XRD analysis, and pp. S59-S79 for details on each structure. In each case, the secondary metal cation is bound in the crown-ether-like site as expected. Within the pairs of structures that feature secondary cations having the same charge, the formal coordination numbers (C.N. values) are in accord with the ions' relative sizes. K^+ adopts C.N. = 9 (see p. S59-S60 for details on this determination) and features a κ^2-triflate, while smaller Na^+ adopts C.N. = 7 and features a κ^1-triflate; similarly, Sr^{2+} adopts C.N. = 9 and features one κ^1-triflate and one κ^2-triflate, while smaller Ca^{2+} adopts C.N. = 8 with two κ^1-triflates. The trivalent cations La^{3+} and Lu^{3+} show similar behaviors, with all three of their accompanying triflate counter-anions bound in all cases; La^{3+} features C.N. = 10 with one κ^2-triflate and Lu^{3+} features C.N. = 9 with three κ^1-triflates. Considering all this data, we conclude that the size of the secondary cations, which can be parametrized through their Shannon ionic radii (see Table 1), influences their coordination behavior within $\mathbf{L_{salmen}}$.

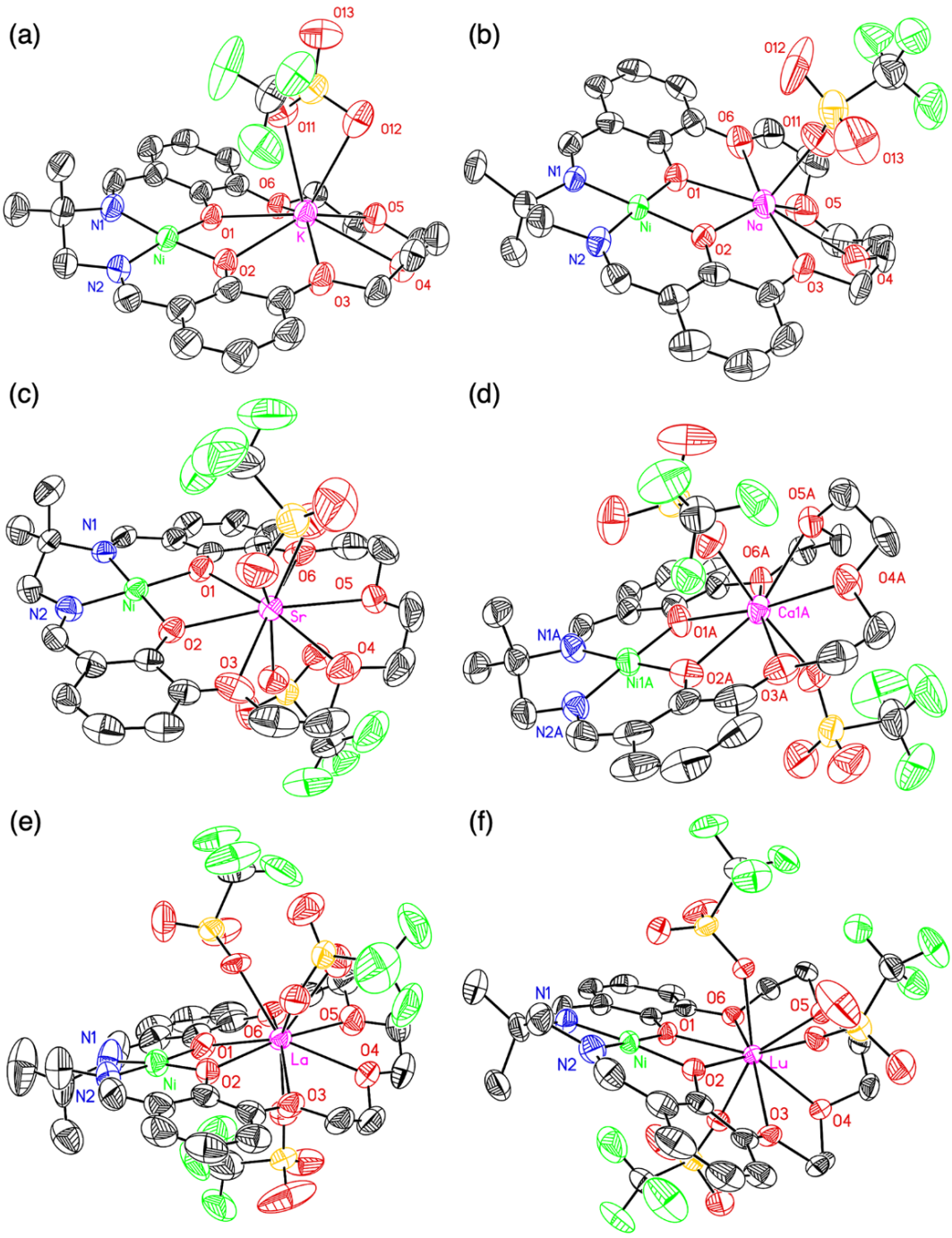

Figure 1. Solid-state structures (XRD) of the heterobimetallic complexes featuring mono-, di-, and trivalent cations. (a) K^+ adduct; (b) Na^+ adduct; (c) Sr^{2+} adduct; (d) Ca^{2+} adduct; (e) La^{3+} adduct; (f) Lu^{3+} adduct. All hydrogen atoms, outer-sphere co-crystallized solvent, and atoms

associated with minor components of structural disorder are omitted for clarity. Displacement ellipsoids are shown at the 50% probability level.

Compound	[Ni] [h]	[Ni,K]	[Ni,Na]	[Ni,Sr] [i]	[Ni,Ca] [i]	[Ni,La]	[Ni,Lu]
pK_a of $[M(H_2O)_m]^{n+}$ [a]	-	16	14.8	13.2	12.6	9.1	7.9
Coordination number (CN) of M	-	9	7	9	8	10	9
Shannon ionic radius of M (Å) [b]	-	1.55	1.12	1.31	1.12	1.27	1.03
$N_1 \cdots N_2$ (Å)	2.544(7)	2.524(4)	2.534(11)	2.51(1)	2.50(3)	2.509(17)	2.537(6)
$O_1 \cdots O_2$ (Å)	2.514(5)	2.522(3)	2.457(9)	2.50(1)	2.46(2)	2.495(9)	2.408(4)
$Ni–N_{imine}$ (Å) [c]	1.869(4)	1.854(3)	1.850(7)	1.84(1)	1.85(2)	1.845(9)	1.846(5)
$Ni–O_{phen}$ (Å) [c]	1.859(4)	1.853(2)	1.842(6)	1.85(1)	1.85(2)	1.862(6)	1.848(3)
$M–O_{phen}$ (Å) [c]	-	2.714(3)	2.393(6)	2.57(2)	2.40(2)	2.522(6)	2.301(3)
$M–O_{3,6}$ (Å) [c]	-	2.790(3)	2.561(8)	2.685(4)	2.60(2)	2.692(5)	2.524(3)
$M–O_{4,5}$ (Å) [c]	-	2.858(3)	2.896(9)	2.688(4)	2.55(2)	2.662(6)	2.434(3)
Ni•••M (Å)	-	3.717(1)	3.426(3)	3.611(3)	3.42(1)	3.561(2)	3.3567(8)
ω_{salmen} [d]	-	0.112	0.002	0.062	0.045	0.066	0.065
ω_{crown} [e]	0.245	0.107	0.353	0.090	0.371	0.194	0.585
τ_4 [f]	0.072	0.098	0.021	0.057	0.047	0.062	0.072
ψ_{Ni} [g]	0.002	0.008	0.008	0.009	0.008	0.023	0.014

[a] From reference 15. [b] From reference 19. [c] Defined as the average interatomic distance between the noted metal and the relevant oxygen/nitrogen atoms. [d] Defined as the root mean square deviation (RMSD) of O1, O2, N1, and N2 from the mean plane of their positions. [e] Defined as the RMSD of the positions of atoms O1, O2, O3, O4, O5, and O6 from the mean plane of their positions. [f] Geometry index for four-coordinate complexes, with a value of 1.00 indicating perfect tetrahedral geometry and zero indicating completely square-planar geometry. Calculated as described in reference 30. [g] Absolute value of the distance between Ni and the mean plane of O1, O2, N1, and N2. [h] From reference 21. [i] Average values for **[Ni,Sr]** and **[Ni,Ca]** were calculated as the arithmetic mean of the values of the parameters in the structural data. Stated e.s.d.'s on distances for **[Ni,Sr]** and **[Ni,Ca]** were taken as the largest of the individual values in the refined data for the particular values corresponding to the given independent molecular species in the refined structural data. See Table S4 for data regarding the independent molecular species.

Table 1. Structural parameters for the heterobimetallic **[Ni,M]** complexes from X-ray diffraction (XRD) analysis.

In the solid-state structures of all the heterobimetallic complexes except that of **[Ni,K]**, the metal-containing complexes do not appear to interact in any significant fashion with each other and display only minimal, noncovalent packing interactions with neighboring species. However, **[Ni,K]** appears to form a weakly bonded dimeric unit in the solid state that is composed of two equivalents of the targeted heterobimetallic complex (see Figure S96). These two equivalents of as-synthesized **[Ni,K]** interact across a crystallographic inversion center; only a single set of atom positions for **[Ni,K]** are defined in the asymmetric unit, but inspection of the environment of **[Ni,K]** reveals pairwise interactions between individual heterobimetallic complexes. The result is a pair of nickel coordination planes slipped to produce a [Ni_2,O_2] parallelogram with "axial" Ni•••O_{phen} distances of 3.57 Å and similarly long Ni•••Ni separations of 3.63 Å. On the one hand, a search of the Cambridge Structural Database[24] for nickel salen or salophen complexes interacting with "axial" oxygen ligands in an intramolecular, bonded fashion revealed Ni•••O distances spanning a range from 1.79 to 2.41 Å.[25,26,27,28] On the other hand, a search of the CSD for intermolecular Ni•••O contacts revealed a span of 2.68 to 3.15 Å; as our Ni•••O is longer than these prior examples at 3.57 Å, the association between heterobimetallic complexes can be concluded to be rather weak. Additionally, we note that our inspection of the CSD revealed that at least two other Ni(salen) structures[29] form similar parallelograms in the solid state with Ni•••O_{phen} distances of 2.84 and 3.11 Å, respectively. In all these cases, the interactions detected between Ni(II) and O_{phen} can be concluded to be primarily electrostatic in nature.

Assembly of the noted parallelogram in our structure (i.e., dimerization of **[Ni,K]**) appears to be further favored by a pair of weak C–H•••K packing interactions that feature long apparent H•••K distances of 2.98 Å. Each of these interaction occurs between one hydrogen (H21B) of the

methylene carbon (C21) in the diimine backbone of **[Ni,K]** and the nearby potassium ion. The C–H•••K interaction is presumably driven by intrinsically weak packing forces, as K^+ ion is not drawn toward the C–H bond but rather sits out of the mean plane defined by the crown ether O atoms on the opposite "face" of the $\mathbf{L_{salmen}}$ ligand by 0.74 Å. The observation that K^+ sits out of the plane could be attributable to the presence of the aforementioned formally κ^2-triflate, which features conventional $K–O_{triflate}$ distances of 2.79 and 3.03 Å, as well as what appears to be a weak $K•••F_{triflate}$ interaction with a distance of 3.26 Å. These interactions appear to assist the triflate ion in occupying the exposed face of the potassium ion, effectively pulling the ion "up" out of the plane of the crown ether and opening space for the nearby methylene C–H moiety to move into the ring of O-atoms defining the crown site. As K^+ is by far the largest ion investigated in our **[Ni,M]** series (see Shannon ionic radii values in Table 1), we anticipate that most of these unique solid-state features are attributable to the relatively large size of this ion in comparison with the size of the crown-ether-like site in $\mathbf{L_{salmen}}$. At this point, however, we note that as all the interactions holding the dimeric species together in the solid state appear weak, upon dissolution in solution, one would anticipate formation of a monomeric species. In the monomeric complex, the polyether chain could reorganize to some extent, rearranging and allowing solvent (MeCN) molecules to bind and fill in gaps in the K^+ coordination sphere in order to achieve a preferred higher coordination number. The triflate could bind in a monodentate or bidentate fashion in solution, or even dissociate to yield a cationic heterobimetallic species (see pp. S59-S60).

Despite these unique solid-state features for **[Ni,K]**, analysis of the structural parameters associated with the Ni(II) ions indicates that the coordination environment of nickel itself is quite consistent across the **[Ni,M]** series. The average $Ni–N_{imine}$ and $Ni–O_{phen}$ distances are similar

(indistinguishable in terms of the 3σ criterion) in all of the complexes (see Table 1 and Figure S118), suggesting that the environment of the Ni center does not change significantly upon incorporation of the secondary metals. The coordination geometry of the Ni center remains rather strictly square-planar in all cases, as judged by the τ_4 geometry indices that remain near zero for all the complexes (see Figure S119).[30] The observation of near-zero τ_4 geometry indices is in accord with quantification of minimal out-of-plane deformation of the N_{imine} and O_{phen} atoms that define the tetradentate Schiff-base [N_2,O_2] cavity (ω_{salmen} parameter, see Table 1). The most significant deviation from square planarity for the Ni center is found in the case of **[Ni,K]**, but this deviation can likely be attributed to minor distortions brought about by the dimerization of **[Ni,K]** in the solid state. The ethylene backbone in the Schiff-base site of $\mathbf{L_{salmen}}$ appears to have sufficient flexibility to enable one C–H moiety (C21–H21B) found on one methyl group of the backbone to embed into the enclosed volume of the nearby and appropriately shifted (inversion-related) crown site, allowing for more efficient, preferable solid-state packing. As a consequence of this interaction, a torsion is induced in the ethylene bridge and thus translates down the chain to the two imine (donor) groups in the Schiff-base moiety; this effectively out-of-plane distortion clearly drives up the ω_{salmen} parameter to 0.112, the highest value of this parameter across the series of complexes **[Ni,M]**. However, in all cases, there is minimal displacement of the nickel center from the plane defined by ligand donor atoms (Ψ_{Ni} parameter, see Table 1), showing that the nickel center remains firmly planted in the Schiff-base-site of $\mathbf{L_{salmen}}$ in all cases. Considering all of these quantitative metrics, the nickel sites in our complexes appear quite structurally consistent in the solid state.

In contrast with the rather narrow range of metrics for the nickel sites, the structural data from XRD analysis show that the behavior of the secondary metal cations held in the crown-ether-like

[O_6] site is far more varied across the series. We first noticed this behavior when inspecting the metal-to-oxygen bond distances for the complexes; we found that, as expected, the cations associated with smaller ionic radii display shorter M–O distances in all cases. Regarding the analysis of the average M–O distances, we note here that the large and potentially planar macrocyclic ligand $\mathbf{L_{salmen}}$ would be C_2- or C_S-symmetric without the two distal methyl groups on the ethylene bridge of the salen-like site. Thus, we examined the average **M**–O_{phen}, **M**–$O_{3,6}$ and **M**–$O_{4,5}$ distances (see Table 1) assuming that the two noted methyl groups would not induce significant structural perturbations across the Ni•••M vector in the heterobimetallic species. As expected, the bond distances and angles from the opposing "sides" of the complexes were found to be similar in each case. The average **M**–O_{phen}, **M**–$O_{3,6}$ and **M**–$O_{4,5}$ distances all display reliable linear dependences on the Shannon ionic radii of the metal cations (see Figure S116).[19] As the oxygen donors are constrained by ethylene linkers within the framework of our macrocyclic ligand, their coordination to **M** forces the polyether to flex (or bow) as it wraps around **M** to (partially) satisfy its preferred coordination number. This behavior can be seen visually in the structures themselves (see Figure 1) but was quantified, as in our prior work, through the ω_{crown} parameter (see Table 1). The tendency toward distortion of the macrocycle particularly affects the smaller cations, as in **[Ni,Na]** (ω_{crown} = 0.353) **[Ni,Ca]** (ω_{crown} = 0.371) and most dramatically, **[Ni,Lu]** (ω_{crown} = 0.585). Thus, the smaller cations can be concluded to distort the structure of the crown-ether-like site more dramatically than their larger analogues within each valency. As expected, the O1, O2, O3, and O6 atoms in each structure are much closer to being coplanar.

Returning to the **M**–O distances, we were intrigued upon close inspection of the data to note that the **M**–O_{phen} distances show the greatest dependency on ionic radius among the three classes of symmetry-related distances. The change in average distance (in Å) normalized by ionic radius

(in Å; see Figure S116) returns unitless dependencies of 0.79(±0.04) for **M**–O_{phen}, 0.77(±0.17) for **M**–$O_{4,5}$, and only 0.51(±0.04) for **M**–$O_{3,6}$. Thus, the most significant change was measured for **M**–O_{phen} and the most modest change was measured for **M**–$O_{3,6}$. This finding is in accord with the flexible nature of the alkyl ether moieties (containing O4 and O5); these atoms have sufficient structural degrees-of-freedom to adopt sterically ideal positions on the coordination spheres for the individual secondary cations. On the other hand, the bridging phenoxides (O1 and O2) and aryl-ether oxygen donors (O3 and O6) are held more tightly in place as they are bonded to sp^2-hybridized carbons within the aromatic portion of the macrocyclic ligand. As a result, the secondary metal cations can draw the alkyl ether donors "inward" while also themselves nestling inward toward the bridging phenoxide donors. As result, the **M**–O_{phen} distances span 0.41 Å in the series, the **M**–$O_{4,5}$ distances span a similar 0.46 Å, and the more rigid **M**–$O_{3,6}$ distances span only 0.27 Å. We hypothesize that the tendency for the metal cations to nestle into the [$Ni^{II}(\mu_2$-$O_{phenoxide})\mathbf{M}^{n+}$] diamond cores is driven by partial anionic character on oxygens O1 and O2, arising from deprotonation of these sites during installation of the nearby Ni(II) center and supporting attractive interactions with the electropositive secondary metal cations.

In accord with these bonding trends for the crown-ether-like site, we have found that the Ni•••**M** distance is linearly dependent on the Shannon ionic radius of the incorporated secondary metal cation. As shown in Figure 2, the smaller metal cations sit closer to the nickel(II) centers in the complexes whereas the larger metal cations prefer to sit at a greater distance away. This behavior was quantified by the slope (unitless) of the relationship, which has the value of 0.70(±0.03); the modest uncertainty on this value corresponds to only 4.3%, in accord with the good correlation displayed in the data (R^2 = 0.99). As the disposition of the Ni(II) center in all the complexes appears fixed based on the preceding analysis in this section, the change in the

Ni•••**M** interatomic separation can be confidently ascribed to changes wrought by the properties of secondary metal cations; these appear dependent on the ionic radius of **M**. In line with these observations, the O1•••O2 separation also displays a highly correlated but non-linear dependence on the ionic radius of **M** (see Figure S120). Thus, the smaller secondary metals draw together O1 and O2 in the complexes, tightening the diamond core motif by nestling more closely into the binding site. And, contrasting with this drawing together of O1 and O2, the N1•••N2 distances remain virtually invariant across the **[Ni,M]** family of complexes due to the ethylene link between them as well as the covalent nature of the nickel site, which appears to have limited structural degrees of freedom. We also note here that although heterobimetallic complexes based on Reinhoudt-type ligands have been studied by our group and others for a number of years, the dependence of M′•••**M** distance on ionic radius has not before been conclusively established through interrogation of a comprehensive series of complexes (cf. Figure S114 in reference 9).

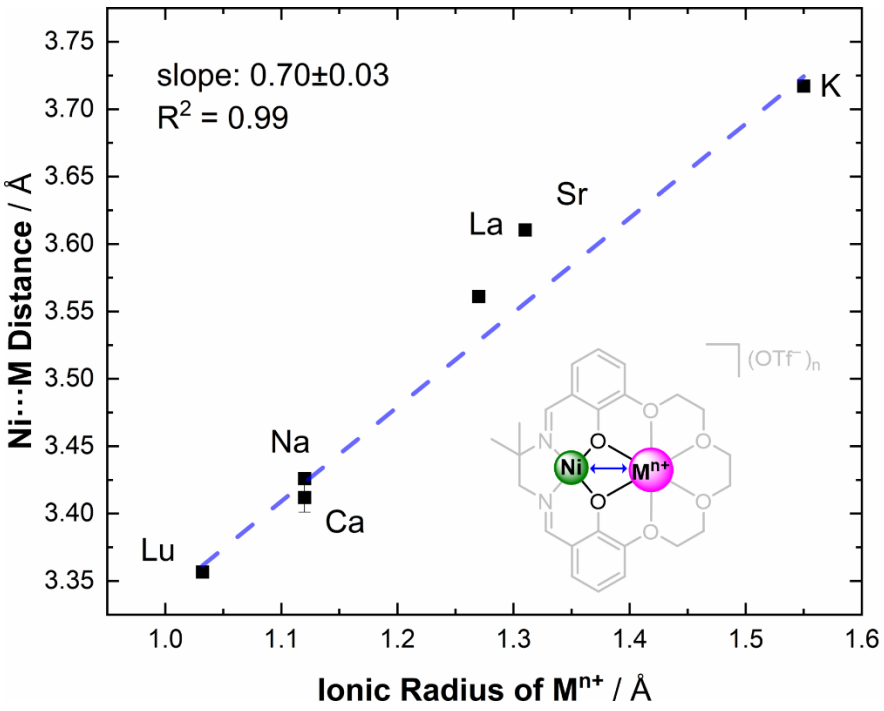

Figure 2. Plot showing the relationship between the Ni•••**M** distance and the ionic radius of $\mathbf{M^{n+}}$. The positive trend shows that smaller ions tend to sit closer to the Ni(II) ion.

Electronic Absorption Spectroscopy. Having observed the significant cation-induced changes in the solid-state structures of the heterobimetallic complexes, we were curious to quantify how the electronic absorption properties of the complexes would be affected by incorporation of the cations. In particular, we were interested in quantification of cation-induced shifts in both charge-transfer (CT) and d-d transitions that are typically observable in square-planar nickel(II) complexes of Schiff-based-type ligands.[31] Regarding identification of these transitions for **[Ni]**, the d-d transition could be assigned as corresponding to the feature near 550 nm, due to its position as well as modest molar absorptivity value (ε = 100 M^{-1} cm^{-1}). The anticipated CT band was found at 418 nm, and was assigned on the basis of its larger molar absorptivity value (ε = 4,500 M^{-1} cm^{-1}). Similar features were measured for all the heterobimetallic species, albeit

shifted in each case to higher energies, similar to observations made in prior work (see Figures S40-S66).[8,9,10]

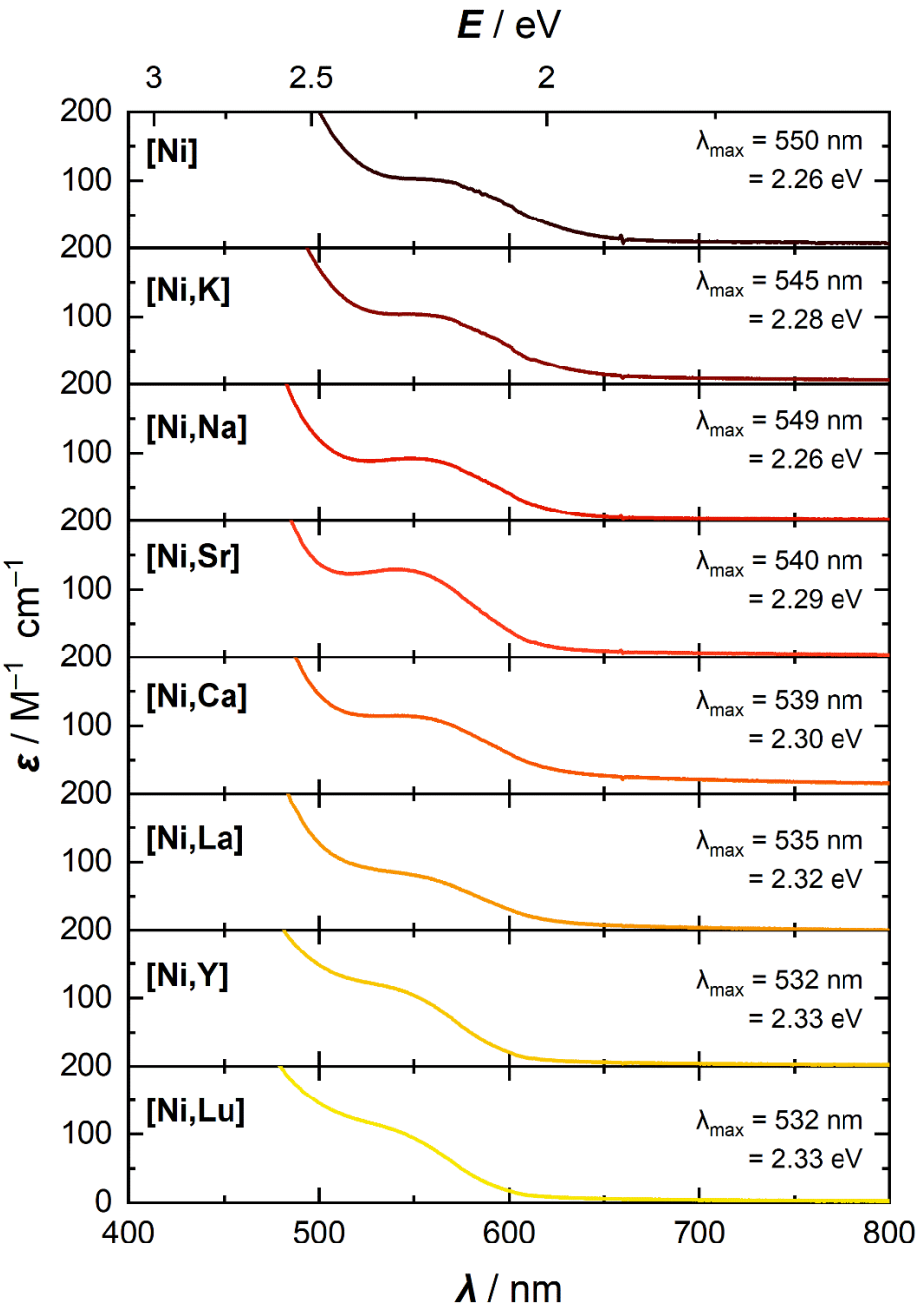

Figure 3. Stacked UV-Visible spectra focusing on the d-d transitions noted for **[Ni]** as well as each compound in the **[Ni,M]** family.

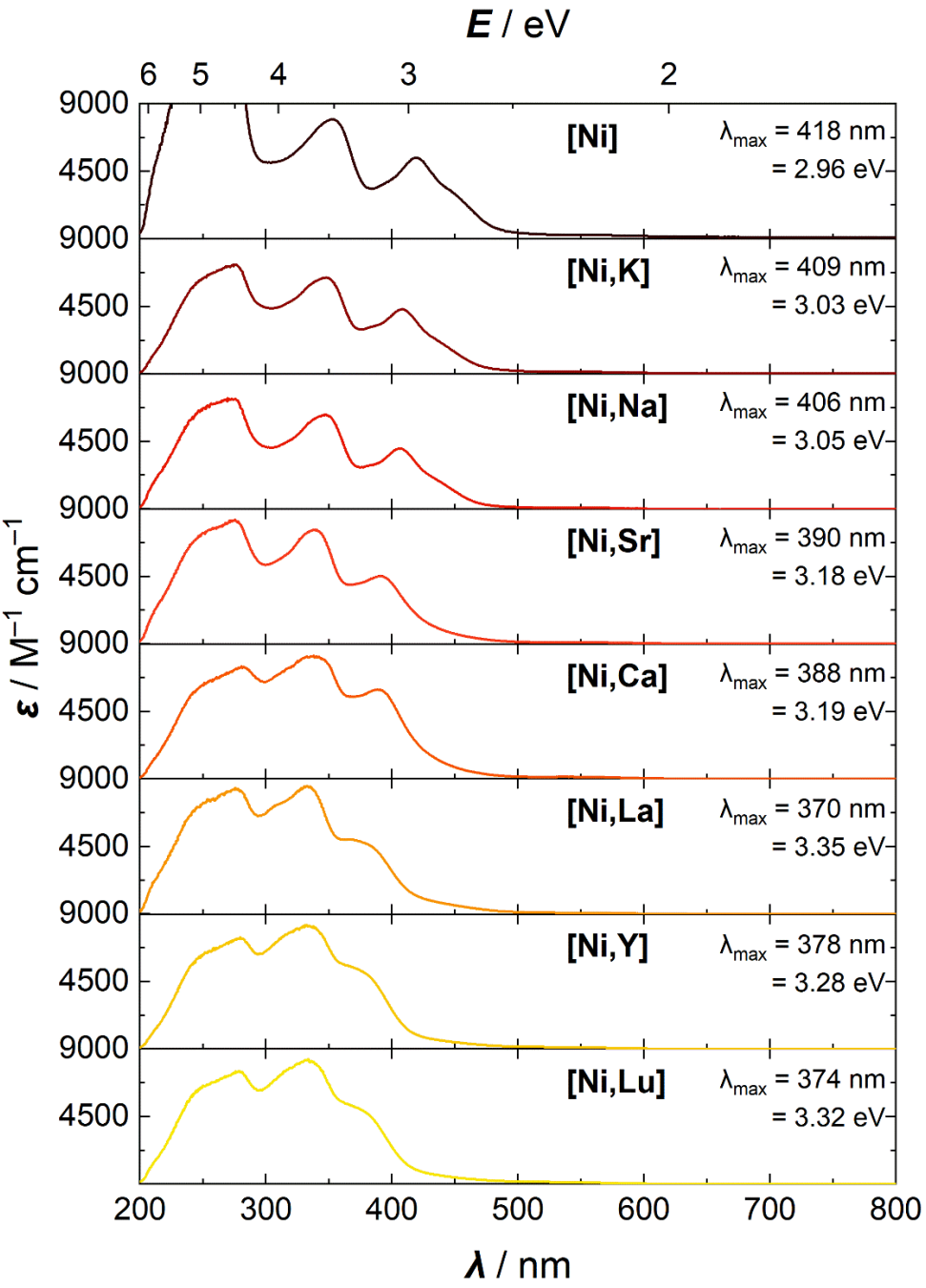

Figure 4. Stacked UV-Visible spectra focusing on the CT transitions noted for **[Ni]** as well as each compound in the **[Ni,M]** family. λ_{max} values for the species incorporating trivalent cations were obtained through peak deconvolution (see SI, p. S33-S37).

Inspection of the measured spectral data for all the complexes revealed that both the d-d transitions and the CT transition energies are blue shifted relative to the precursor complex **[Ni]**. As shown in Figure 4, the CT transitions undergo a shift from 418 nm for **[Ni]** to 370 nm for **[Ni,La]** whereas the d-d transitions shift more modestly from 550 to 535 nm for the same range of complexes as seen in Figure 3. Plotting the energies of both the CT and d-d transitions as functions of the Lewis acidity values (pK_a values of the respective aqua ion) corresponding to each secondary metal cation reveals a reasonable linear dependence in each case (Figure 5). Examination of the quantitative dependences of the transition energy shifts on the pK_a values reveals that the shift of the CT band is –36 ± 5 meV/pK_a. On the one hand, this value is similar to those that we have measured in analogous systems supported by $\mathbf{L}_{\mathbf{salmen}}$ featuring the vanadyl ion[10] (VO^{2+}; –30 ± 5 meV/ pK_a) and palladium(II)[9] (–45 ± 3 meV/pK_a). The similarity of these observations is attributable in part to the use of the same $\mathbf{L}_{\mathbf{salmen}}$ ligand backbone in all these works. On the other hand, the d-d transition energy was found to be markedly less sensitive to the effects of the secondary metal, quantified to be only –7.7 ± 1.3 meV/pK_a. This suggests that the energy levels of the individual donor and acceptor orbitals involved in the d-d transition are affected similarly by the presence of the secondary metal cations, whereas the orbitals involved in the CT transitions are more differentially affected.

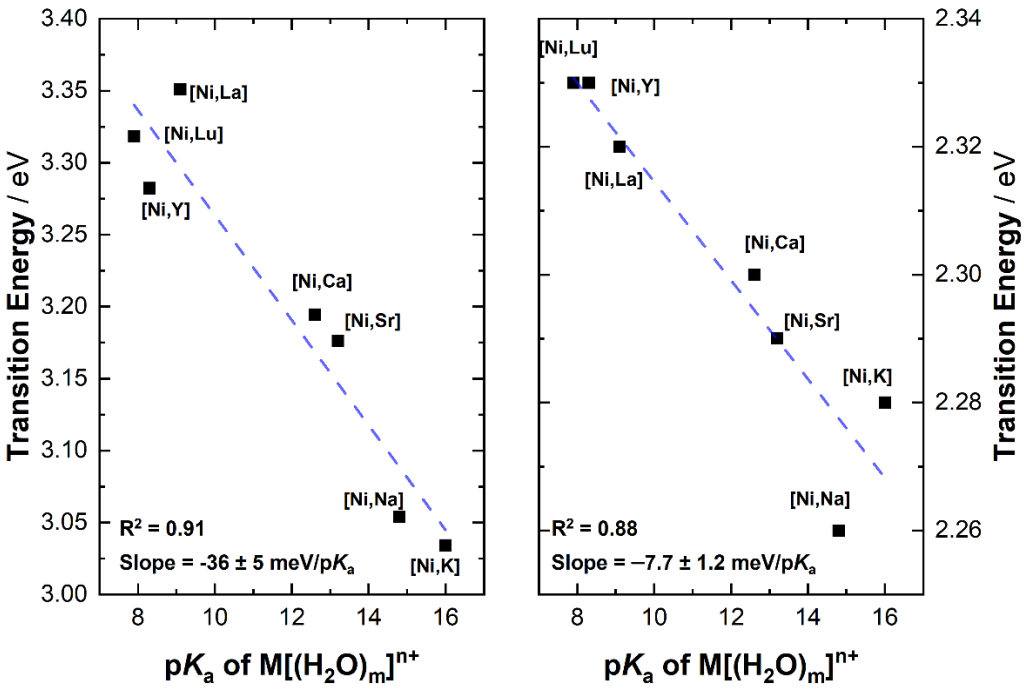

Figure 5. Plots showing the dependence of the studied transitions (left, CT; right, d-d) of **[Ni]** and the **[Ni,M]** family on the Lewis acidity of the associated secondary metal.

The observation of a modest dependence of the d-d transition energy for the **[Ni,M]** series of complexes studied here contrasts with the much more significant shift encountered for the case of the analogous series of vanadyl complexes mentioned above. In particular, we note that the shift of a d-d feature for the vanadyl complexes underwent a cation-driven tuning shift of −50 ± 10 meV/pK_a.[10] This value is over 7x greater than that found for the nickel(II) complexes studied here. In terms of the d-d transitions being measured in each case, examination of the literature suggests that, for square-planar nickel(II) complexes, the highest energy (empty) orbital is conventionally assigned as $3d_{x2\text{-}y2}$ or $3d_{xy}$, depending on the orientation of the x and y axes relative to the four in-plane ligands.[31] The four filled lower energy orbitals are often so close

together in energy that individual transitions from these orbitals to the empty, upper 3*d*-level cannot be distinguished, leading to the single transition measured here. For the vanadyl complexes that feature a $3d^1$ configuration in all cases, the spectral data are impacted by the strong axial perturbation caused by the terminal [V–O_{oxo}] group. There are three potential intra-*d*-shell transitions in vanadyl complexes, although not all are necessarily allowed and their assignments in individual complexes have long been the subject of controversy.[32] In the spectra of the vanadyl complexes under comparison here, there are two apparent transitions in a closely-spaced manifold of absorption intensity; we have previously referred only to the overall shift in this manifold as judged by the λ_{max} value corresponding to the wavelength of maximum absorption for the full manifold. In both the vanadyl and nickel(II) complexes, however, we note that the estimated energies of the d-d transitions can be compared, as they should serve as a measure of the changes wrought on the metal-centered orbitals by the secondary metal cations.

The origin of the modest shift of the d-d transitions for the nickel(II) complexes reported here in comparison to that of the previously reported vanadyl complexes can be identified on the basis of the available solid-state structural data. For the nickel(II) complexes, the Schiff-base binding site where the nickel center is located in the complexes is structurally rather invariant across the full series of complexes. The site remains rigorously square planar (as quantified by the τ_4 geometry index) and the metal center remains firmly bound in the plane defined by N1, N2, O1, and O2 (as quantifed by the ψ_{Ni} parameter). The average Ni–O_{phen} and Ni–N_{imine} distances shift very little across the full series of Lewis acid adducts; for example, the Ni–O_{phen} distances are similar for **[Ni]** (1.859(4) Å) and **[Ni,Lu]** (1.848(3) Å). Conversely, the vanadyl moiety in the **[VO,M]** complexes undergoes significant structural changes upon incorporation of secondary metal cations into the monometallic precursor denoted **[VO]**. For example, the average V–O_{phen}

distance elongates from 1.924(1) Å for **[VO]** to 1.94(1) Å for **[VO,Ca]**. Moreover, the V–O_{oxo} bond shortens upon incorporation of Na^{+} or Ca^{2+}, shifting from 1.605(1) Å in **[VO]** to 1.595(7) in **[VO,Na]** and 1.59(1) Å in **[VO,Ca]**. These changes in the coordination environment about the vanadium center could contribute to the more dramatic changes in the UV-visible spectra; in particular, the contraction of the V–O_{oxo} distance should allow the oxo ligand to serve as a stronger σ- and π-donor, widening the span of d-orbital energies and driving the noted blue shift in the absorption spectra. The nickel case thus contrasts from the perspective that the coordination environment about the metal remains more invariant across the series of secondary cation adducts, resulting in more similar d-d transitions across the series of complexes. In accord with this model, however, the CT energies shift more dramatically in the nickel(II) complexes; this can be ascribed to a stronger influence of the secondary cations on the occupied metal orbitals in comparison with a more modest influence on the empty ligand-centered acceptor orbitals. This situation drives the more significant blue-shift in the CT energies as measured in the data, and is consistent with prior analyses on nickel,[5] palladium,[9] and zinc complexes[33] from our laboratory.

Electrochemical Studies. In our past work on redox-active heterobimetallic complexes, analysis of both thermodynamic and kinetic considerations has been complicated by follow-up chemical reactivity associated with redox cycling. For example, in prior work on heterobimetallic nickel complexes, the Ni(II)/Ni(I) reduction of interest was essentially irreversible, precluding chemical studies of the reduced forms of the complexes.[5,34] Similarly, we found cation-dependent behaviors when studying the V(IV)/V(V) oxidation for our **[VO,M]** complexes, suggesting that the complexes undergo speciation, perhaps by loss of the secondary metal cations, upon oxidation.[8] The use of the $\mathbf{L_{salmen}}$ ligand system in the present work, however,

helped us to avoid such complications; nickel(II) compounds based on salen-type ligands have been known for many years to display a chemically reversible reduction wave in cyclic voltammetry.[12,35] We have found this to be true in the case of the full series of **[Ni,M]** complexes, setting the stage for thorough characterization of the electron transfer properties of these complexes in this work. And, it should be noted that all past studies from our group aimed at interrogation of the properties of adducts with trivalent cations have been impacted by irreversible electrochemical behaviors.[5,8,9,10,33,36] This motivated the present study, in that proper characterization of trivalent cation adducts could produce evidence of the factors enabling these strongly Lewis acidic species to engender unique properties.

Starting with the monometallic precursor complex **[Ni]**, cyclic voltammetry (CV; see Table 2) revealed a quasi-reversible couple centered at $E_{1/2}$ = –2.14 V vs. the ferrocenium/ferrocene couple (hereafter denoted as $Fc^{+/0}$). Both the cathodic and anodic waves remain observable across the multiple scan rates utilized here (see Figure S70), in accord with formation and persistence in solution of a $1e^-$ reduced form of the complex featuring a nickel(I) metal center; the electrogenerated nickel(I) complex persists on the timescale of the CV experiment. Appealingly, scan-rate-dependent studies over the range of 50-1000 mV/s confirmed freely diffusional behavior at the electrode for both the oxidized and reduced forms of the compound; this is consistent with the good solubility of the complex in MeCN-based solutions. Additionally, we note here that the peak-to-peak separation of the cathodic and anodic waves (hereafter denoted ΔE_p) was found to be 84 mV when measured at 100 mV/s, consistent with relatively fast electron transfer behavior in our organic electrolyte.[37]

Compound	pK_a of $[M(H_2O)_n]^{n+}$ [a]	$E_{1/2}$ (V)	$\Delta E_{1/2}$ vs [Ni] (mV)[b]	ΔE_p (mV)[b]	k^0 (cm/s * 10^3)[c]	$\%V_f$
[Ni]	-	–2.14	0	84	6.4±0.3	45.8
[Ni,K]	16	–1.95	190	82	7.9±0.3	36.5
[Ni,Na]	14.7	–1.95	190	77	7.4±0.6	39.6
[Ni,Sr]	13.2	–1.68	460	81	8.1±0.3	37.4
[Ni,Ca]	12.7	–1.68	460	78	8.2±0.3	36.5
[Ni,La]	9.1	–1.42	720	88	6.2±0.3	30.7
[Ni,Y]	8.3	–1.45	690	103	3.7±0.2	-
[Ni,Lu]	7.9	–1.43	710	110	3.5±0.2	24.5

[a]From reference 15. [b]Measured at 100 mV/s. [c]Average value reported is the arithmetic mean of the values determined at eight different scan rates (50, 100, 150, 200, 250, 300, 500, and 1000 mV/s). Uncertainty (reported as ±1σ) was calculated from the replicate data.

Table 2. Electrochemical characteristics of **[Ni]** and the **[Ni,M]**.

With the electrochemical profile of **[Ni]** in hand, we proceeded to similarly interrogate the heterobimetallic complexes to check for any relationship between the identity of the incorporated secondary metal cation and its effect on the thermodynamic nickel(II)/nickel(I) potential. Each redox couple of this type measured for the complexes in the **[Ni,M]** family exhibited reversible reductions similar to that of **[Ni]**, albeit shifted to more positive thermodynamic potentials as seen in Figure 6. This behavior qualitatively matches prior fundings from Yang and co-workers on mono- and di-valent cation adducts,[12] as well as our work on related nickel complexes based on a more highly conjugated ligand system denoted $\mathbf{L_{salben}}$.[5] In line with this prior work, the

thermodynamic $E_{1/2}$ values shift in a predictable fashion based on the charge (rather than Lewis acidity or another descriptor) of the incorporated secondary metal cation. The monovalent and divalent cations display identical $E_{1/2}$ values of –1.95 V and –1.68 V, respectively, and the trivalent cations display very similar $E_{1/2}$ values spanning a narrow range from –1.42 V to –1.45 V. In all cases, the oxidized and reduced forms of the complexes were shown through scan-rate-dependent studies to be freely diffusional at the working electrode surface, confirming there is no apparent influence on this data of secondary surface adsorption or chemical reactivity phenomena (see pp. S41-S48).

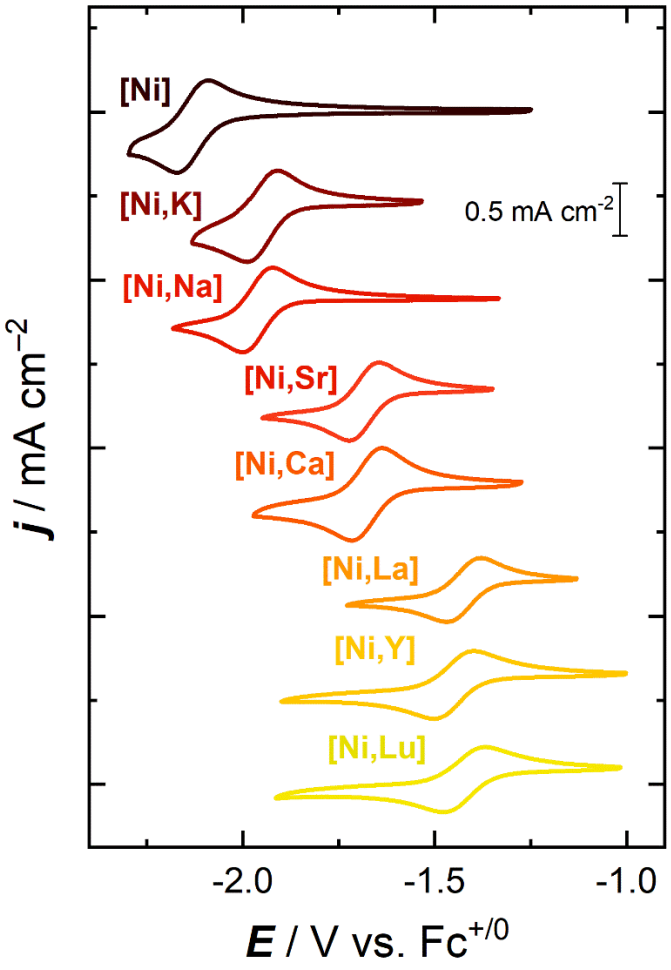

Figure 6. Stack of the cyclic voltammograms from **[Ni]** and the **[Ni,M]** family. All scans were taken at a scan rate of 100 mV/s at a concentration of 2 mM in acetonitrile (0.1 M $TBAPF_6$).

On the one hand, the observation of charge-dependent reduction potentials for the **[Ni,M]** complexes is in accord with prior literature, particularly works showing that heterobimetallic effects can be understood in the context of electrostatic effects.[12] On the other hand, we were surprised to measure only charge-dependent behavior since the electronic absorption spectroscopy was consistent with clear, Lewis-acidity-dependent changes in *d*-orbital energies

(Figures 3 and 5). We had anticipated that this acidity-dependent behavior would be translated into the electrochemical work as well. Other systems undergoing metal-centered redox that we have studied also showed strong *linear* correlations between reduction potentials and secondary-cation Lewis acidities (as judged by the pK_a values of the corresponding aqua complexes) rather than charge-dependent behaviors.[5,8,9,10,36,38] Plotting the reduction potential values as a function of the Lewis acidity (pK_a values) of the corresponding secondary metal cations in the data reported here, however, reveal a clear "stair-step" appearance in the data (see Figure 7), wherein the data points are clustered according to the charges on the secondary metal cations rather than uniformly across the range according to Lewis acidity. Our prior work on the redox chemistry of heterobimetallic complexes that undergo ligand-centered reduction events do not display this "stair-step" behavior, suggesting that Lewis acidity can be a useful concept to consider in work of this type.[33] Moreover, we note that the slope of the apparent dependence on Lewis acidity in the data below is –69±7 mV/pK_a, a very similar value to that measured in our prior work on nickel complexes[5] (–70±12 mV/pK_a) and also work on heterobimetallic uranyl complexes (–61±9 mV/pK_a).[8] On the other hand, the magnitude of the slope measured here is significantly greater than those we have measured for ligand-centered reduction process in heterobimetallic palladium[9] and zinc[33] complexes of –41±3 and –48±3 mV/pK_a, respectively .

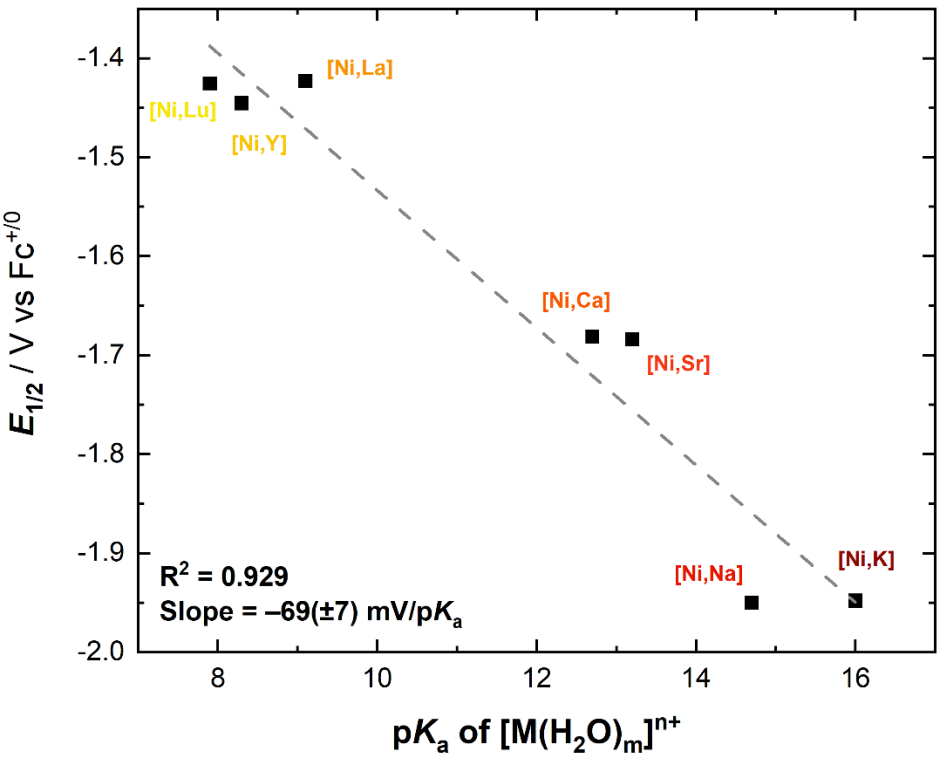

Figure 7. Plot of the $E_{1/2}$ of the **[Ni,M]** family vs. the pK_a value of the relevant M aqua complexes. Notably, charge appears to be the dominant factor in determining $E_{1/2}$.

Clearly, secondary metal cations can induce reproducible effects in heterobimetallic complexes, particularly when the cations are bound in similar locations relative to the moieties undergoing reduction/oxidation. This reliable behavior has inspired a great deal of our work in recent years. However, as the present study is supported by a wealth of structural data, we have been able to conclude here for the first time that the positions adopted by the secondary metal cations depend on the nearby ligands (especially the bridging phenoxide moieties in our complexes) and the identity of the cation in question. As any 1e⁻ reduction potential is dependent upon the properties of both the oxidized and reduced forms of the complex being studied,[39] this

raises the question of how reduction (or oxidation) affects the nature of the interaction(s) between the secondary metal cations and the redox-active core of the complexes. We anticipate that the lack of characterization data for the reduced forms of the complexes in this study, and others that have appeared in the literature in the past, could cloud interpretation of thermodynamic redox properties. This is because the reduction potential measured for the isolated nickel(II) complexes in the **[Ni,M]** family actually depend on both the properties of the nickel(II) forms of the complexes as well as on the properties of their reduced counterparts (in the virtually Nernstian system) that feature the nickel(I) oxidation state. Reorganization of the complexes, particularly movement of the cations bound in the crown sites, could give rise to unpredictable effects driven by addition or removal of an electron. Consequently, before continuing our analysis of the cation-dependent properties of the **[Ni,M]** complexes, we sought to directly confirm the generation of Ni(I) species through spectroscopy.

Electron Paramagnetic Resonance Studies. In light of the importance of the properties of the reduced forms of the **[Ni,M]** complexes reported here, we pursued X-band electron paramagnetic resonance (EPR) characterizations that could provide evidence for metal-centered reduction and generation of nickel(I) form(s) of the complexes. Each of the isolated nickel(II) complexes in our study is diamagnetic, featuring a $3d^8$ configuration and $S = 0$ ground state. However, the $1e^-$ reduced forms of our complexes could be anticipated to be paramagnetic in nature, with $3d^9$ configurations and $S = 1/2$ ground states in each case. (All of the secondary metal cations used here are intrinsically diamagnetic.)

Treatment of **[Ni,Lu]**, **[Ni,Ca]** and **[Ni,K]** with 1 equiv of Cp^*_2Co ($E_{1/2} = -1.91$ V in MeCN[40]) resulted in the appearance of new signals in all cases that are consistent with generation of nickel(I).[41] Appealingly, the oxidized form of our chemical reductant is the diamagnetic species

$[Cp^*_2Co]^+$; this species does not contribute any signals to the EPR data, simplifying interpretation of the spectra. In the cases of the spectra obtained upon reduction of **[Ni,Lu]** and **[Ni,Ca]**, the distinctive isotropic signal near g = 1.8 associated with the chemical reductant Cp^*_2Co (see Figure S93) was completely absent, consistent with complete electron transfer to the nickel complexes in these two cases. This is consistent with the measured electrochemical data, in that the reduction potentials for these two complexes are well positive of that for Cp^*_2Co ($\Delta E_{1/2}$ = 0.47 V and 0.22 V, respectively). For **[Ni,Lu]**, a relatively narrow set of features was observed between g = 2–2.1. For **[Ni,Ca]** a similar result was obtained, although there appear to be two overlapping sets of spectral features between g = 2–2.1. In the case of the spectrum obtained upon treatment of **[Ni,K]** with 1 equiv of Cp^*_2Co, a more complex set of features was observed that include a contribution of the unreacted, Co(II) form of Cp^*_2Co. However, there is a clear new set of signals in the data between g = 2–2.3, consistent with electron transfer to generate nickel(I) species. Notably, this is consistent with the measured reduction potential for **[Ni,K]** at –1.95; this potential, although negative of the formal potential for $Cp^*_2Co/Cp^*_2Co^+$ redox, is close enough to support partial reduction of the nickel complex upon exposure to 1 equiv of this chemical reductant (theoretically near 50% on the basis of the electrochemical data).

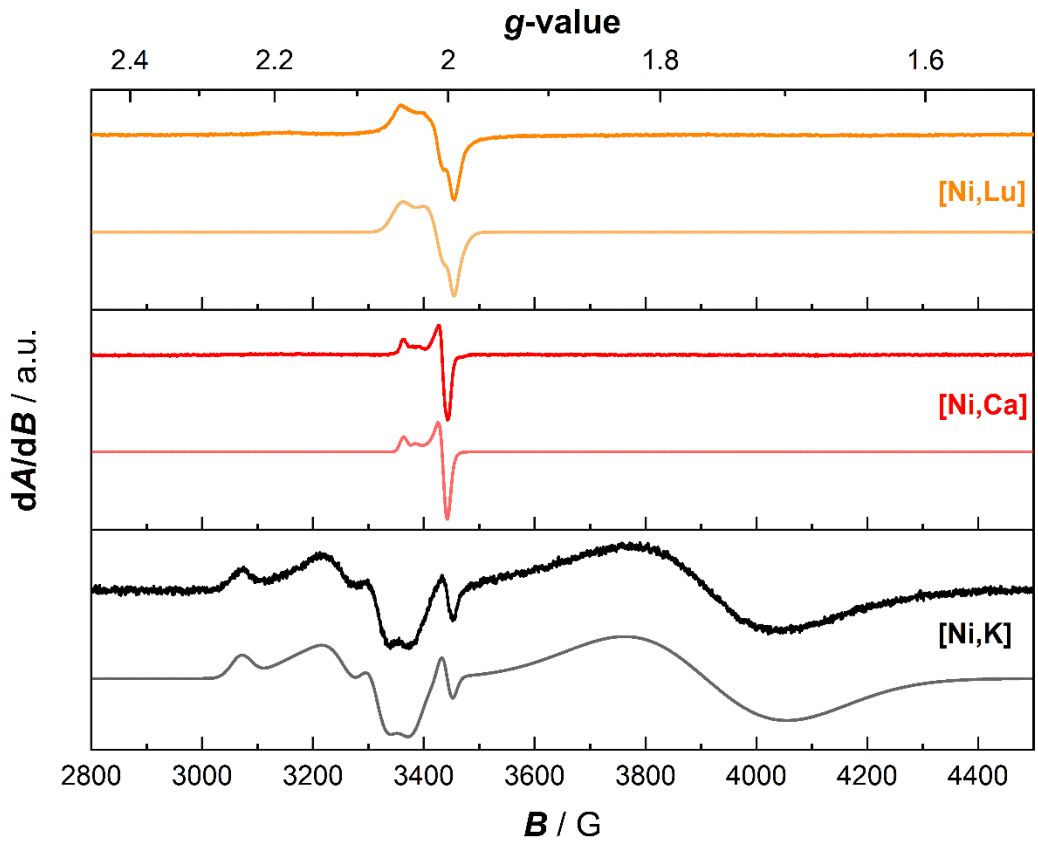

Figure 8. X-band continuous-wave EPR spectra of **[Ni,Lu]** (orange; simulated spectrum in light orange), **[Ni,Ca]** (red; simulated spectrum in light red) and **[Ni,K]** (black; simulated spectrum in gray). The experimental spectra were collected in frozen acetonitrile at ca. 4 K.

The experimental EPR spectra of the *in situ* reduced species could be successfully modeled (see Figure 8) by using the EasySpin software package[42] to confirm the qualitative interpretation of the data given above. The spectral profile of the data corresponding to reduction of **[Ni,Lu]** was well reproduced by a single $S = 1/2$ system displaying axial symmetry and exhibiting g values that are consistent with examples of previously characterized nickel(I) species.[41] A small feature apparent at $g = 1.997$ could be modeled as a small $S = 1/2$ organic radical species, either

arising from decomposition of **[Ni,Lu]** or adventitious contamination of the sample; 98% of the spectral intensity in the model is attributable to reduced nickel(I) while 2% is attributable to the minor organic radical. The data corresponding to reduction of **[Ni,Ca]** could be similarly modeled, revealing that the spectrum could be well reproduced by using a mixture of two components; in this case, both components are S = ½ systems displaying axial symmetry. Component I (77%) has main features at the g-values of 2.048 and 2.003, whereas Component II (23%) has one unique feature at g = 2.035 and a second feature that overlaps with the spectral feature of Component I at g = 2.003. Both of these components are consistent with nickel(I) species, and at this stage, we anticipate that the observation of multiple forms of nickel(I) is attributable to possible triflate ligand loss from the reduced form of the compound; the nickel(I) form of **[Ni,Ca]** is formally anionic, and thus it could have the propensity to lose one triflate upon reduction.

The EPR spectrum obtained upon *in situ* reduction of **[Ni,K]** could also be successfully modeled with EasySpin, although this spectrum was more rich in individual features that the other two in this study. The final model for this spectrum included four individual components, including most importantly a Ni(I) S = ½ system displaying axial symmetry with features at g = 2.242 and 2.102 (Component I; 7%)) and a S = ½ rhombic system with signals at 2.171, 2.078 and 2.040 (Component II; 10%) that could be assigned as nickel(I) species. On the basis of the similar axial features encountered for both these components in comparison to those measured for *in situ* reduction of **[Ni,Ca]**, we anticipate that they arise from nickel(I) species that either retain or lose the triflate counteranion that is bound to the K^+ center in the **[Ni,K]** starting material. Beyond these signals, the broad signal near g = 1.762 could be modeled and assigned as arising from unreacted Cp^*_2Co (corresponding to 83% of the spectral intensity) and a very sharp

signal located at g = 2.001 could be modeled and assigned as an S = 1/2 organic radical species (<1%). At this stage, we anticipate that this organic radical component arose either from minor decomposition of the nickel(I) form of **[Ni,K]** or represents adventitious contamination of the sample. Regardless, these data confirm that the nickel(I) oxidation state is accessible in all three of the samples tested and are in accord with our assignment that the redox process measured in the electrochemistry corresponds to a chemically reversible nickel(II)/nickel(I) process in each case. The observation of a significant portion of unreacted Cp^*_2Co in the spectrum collected for **[Ni,K]** is also in accord with the rather negative reduction potential of this complex ($E_{1/2}$ = –1.95 V).

Determination of Heterogeneous Electron Transfer Rates. Having established the accessibility of the nickel(I) oxidation state for all of the heterobimetallic systems reported here, we were intrigued to note from our electrochemical experiments that the peak-to-peak separation of the cathodic and anodic waves corresponding to Ni(II)/Ni(I) redox are greater for the three adducts of trivalent cations (La^{3+}, Y^{3+}, and Lu^{3+}) than for any of the other complexes studied. Additionally, these waves appear more broadened than for the adducts of weaker Lewis acids (see Figure S85). As demonstrated in the foundational work from Nicholson[43] and described by Savéant and Costentin in their valuable text,[39] an increase in peak-to-peak separation for redox couples measured under identical conditions and displaying similar diffusion coefficients can be attributed to diminished values of the rate of heterogeneous electron transfer (defined as k^0). Diminished values of k^0, generally speaking, are attributable to diminished exchange current densities and processes involving significant molecular reorganization upon electron transfer.[37]

To quantify this phenomenon, the heterogeneous electron transfer rates (k^0) associated with each Ni(II)/Ni(I) couple were determined using the traditional method from Nicholson that relies

on a standard working curve that relates the measured ΔE_p values to k^0. To confirm the precision of our measurements, the values of k^0 were measured at eight different scan rates and tabulated as an average value (see Table 2). The values of k^0 were found, as expected, not to be virtually invariant with scan rate (see Figure S86). With this method we found the k^0 value for **[Ni]** to be a relatively fast at 6.4±0.3 cm s^{-1}, while the value for **[Ni,Lu]** was cut almost in half to 3.5±0.2 cm s^{-1}.

Examining the k^0 values as a function of the pK_a values corresponding to the aqua complexes of the incorporated secondary metal cations, there appears to be a monotonic relationship in the data (see Figure 9). In particular, the k^0 values for the heterobimetallic complexes containing mono- and divalent secondary metals appear in the data as a "plateau" region; based on the precision of our measurements, the k^0 values for these complexes are essentially indistinguishable, a finding in accord with essentially "fast" electron transfer behavior at the electrode surface. On the other hand, incorporation of the trivalent metals slows the rate of electron transfer more modestly for **[Ni,La]** (6.2±0.3 cm s^{-1}) and more dramatically for **[Ni,Y]** and **[Ni,Lu]** (3.7±0.2 and 3.5±0.2 cm s^{-1}, respectively). Consequently, a factor associated with incorporation of the strongly Lewis acidic trivalent cations appears to drive diminished electron transfer rates to the heterobimetallic complexes in the **[Ni,M]** series.

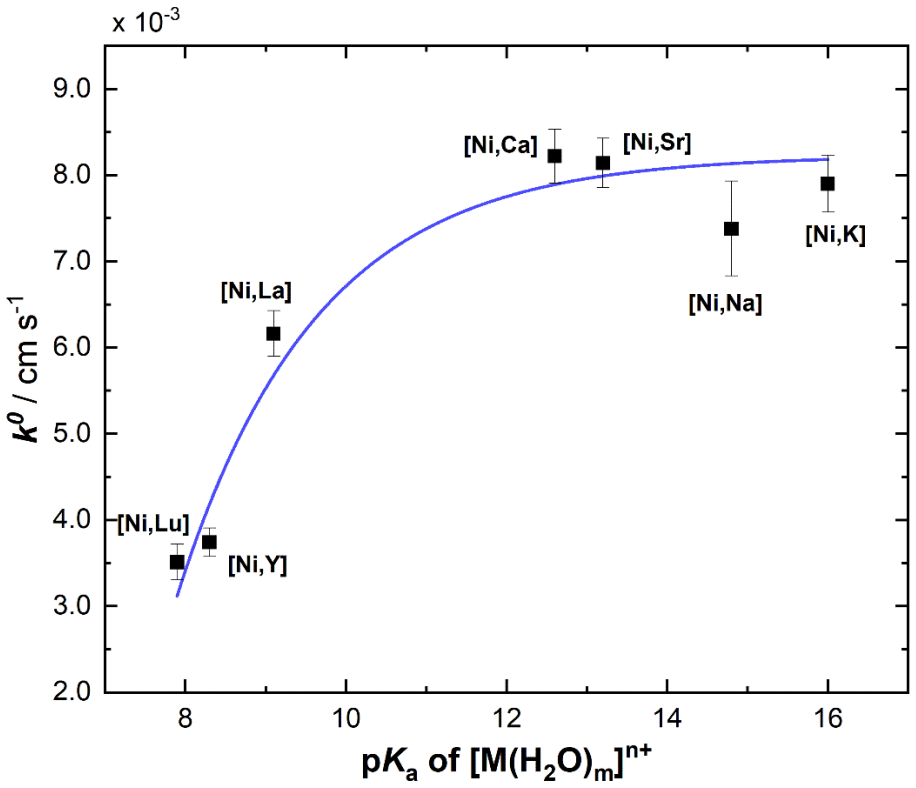

Figure 9. Plot of the heterogeneous electron transfer rate k^0 for the **[Ni,M]** complexes vs. the pK_a of the corresponding M aqua complex. Values and uncertainty were determined as described in Table 2.

Topological Map Generation and Analysis of Steric Congestion. Upon observation of the trend given in Figure 9, we were struck that the dependence on Lewis acidity was markedly distinct from that found during examination of the thermodynamic reduction potential data ($E_{1/2}$ values; Figure 7). Superficially, it was not obvious to us why the more Lewis acidic trivalent cations would induce a slowing of the electron transfer rate to the relevant heterobimetallic complexes. In prior work, however, we have quantified the reorganization energy associated with ligand-centered reduction of a related family of heterobimetallic palladium(II) complexes

based upon the same $\mathbf{L_{salmen}}$ ligand as the **[Ni,M]** series reported here.[9] In that work, the reorganization energy (λ) was found to increase as a function of the Lewis acidity of incorporated secondary metal cations. As smaller values of λ are associated with faster electron transfer (quantifiable through k^0), these prior measurements provide an example closely related to the current work but offer no molecular-level explanation as to the origin of the phenomenon. However, with solid evidence that incorporation of secondary, redox-inactive metal cations into Reinhoudt-type ligand systems can modulate the resulting complexes' electron transfer rates, we looked back at our comprehensive data from X-ray diffraction analysis to search for a structural influence of the trivalent cations that could give rise to this particular behavior.

We began our analysis with the postulate that the region near to the nickel centers in our complexes would be the most important for investigation. This idea is supported by the results of our EPR studies, which support that Ni(II)/Ni(I) redox is responsible for the reduction waves measured in the electrochemical data for the complexes. Consequently, we anticipated that the electron transfer behavior of the complexes would be most affected by the microenvironments (first and secondary coordination spheres) near the nickel centers in each of the heterobimetallic species. With these regions in our minds, we revisited the structural data from single-crystal X-ray diffraction analysis (see Figure 1 and pp. S57-S87 for details). The first coordination spheres in the complexes are highly similar to each other in terms of bond distances to the two imine-nitrogen and two phenoxide-oxygen atoms, as described above. Looking beyond these close contacts that were found for all the heterobimetallic complexes, only the structure of **[Ni,Lu]** revealed another possible covalent interaction of the nickel center with a donor ligand; one triflate (associated with S2) could be serving in the solid state as a bridging ligand between the nickel and lutetium centers. In particular, there is a potential weak interaction (2.908(6) Å)

between the nickel center and a triflate O-atom (O23). This interaction is reminiscent of a similar potential bridging triflate motif that we observed in prior work with a **[Ni,Y]** complex based on the salben ligand (a macrocyclic salophen species) and that featured a similarly short Ni•••$O_{triflate}$ distance of ca. 2.786(7) Å.[5] For context, a search of the Cambridge Structural Database[24] to examine intermolecular contacts between Ni in a Schiff-base-type ligand environment and O atoms at distances of 1.75 to 4.00 Å revealed 292 hits with Ni•••O distances spread across the entire range with, of course, more entries on the long distance end of the range. As mentioned above, a more specific search for nickel salen or salophen complexes interacting with axially bound fifth ligands to nickel revealed only four examples with Ni•••O distances spanning a narrower range of distances from 1.79 to 2.41 Å.[25,26,27,28] Thus, the distance of 2.908(6) Å in our complex appears rather long. We anticipate that this Ni•••O23 contact in the solid-state structure of **[Ni,Lu]** represents a marginal electrostatic interaction rather than a strong dative bond. This conclusion is supported by the formal $18e^-$ count of the Ni(II) metal center with only four covalently bound donor ligands. Thus, we anticipate at this stage that the Ni•••O23 contact in the structure of **[Ni,Lu]** arises from an interaction derived from other influences rather than a significant bonding preference with Ni(II).

Instead of a bonding preference at Ni(II), the coordination properties of our heteroditopic macrocyclic ligand $\mathbf{L_{salmen}}$ appear to drive the increase in steric congestion about the nickel site upon binding of trivalent cations in the crown-ether-like site. Inspection of the crystallographic data shows that there is a structural consequence of the dependence of the Ni•••**M** separation on ionic radius that is shown in Figure 2. This consequence also results from the high coordination numbers associated with the trivalent cations (C.N. = 9 for **[Ni,Lu]** and 10 for **[Ni,La]**), in that two of the bound triflate counteranions in both the structures of **[Ni,Lu]** and **[Ni,La]** appear to be

forced into cantilever-like positions above and below the plane defined by the Schiff-base site containing nickel. In the case of **[Ni,Lu]**, O23 and F13 are located, respectively, 2.908(6) and 3.054(7) Å away from the nickel center on opposite sides of the macrocyclic complex. In the case of **[Ni,La]**, atoms F32 and O23′ are located, respectively, 3.30(1) and 3.70(3) Å from nickel. The two next-shortest contacts for the other complexes between the Ni centers and triflate-associated atoms are 3.80(1) Å for O11B (3.855(8) Å for O11A) in **[Ni,Ca]** and 3.951(4) Å for F13 in **[Ni,K]**. K^+ features a larger ionic radius than Lu^{3+} and La^{3+}, and **[Ni,K]** resembles these complexes in that it also features a high C.N. of 9 (see p. S59-S60 for discussion); this highlights the importance of higher coordination numbers in amplifying steric crowding in these systems. As the crown-ether-like site is located adjacent to the Schiff-base site where Ni(II) binds to $\mathbf{L_{salmen}}$, decreased Ni•••M separation can allow the triflate counteranions to enter the secondary coordination sphere near the Ni(II) center; this effect is enhanced by the macrocyclic nature of the $\mathbf{L_{salmen}}$, as the crown ether is moved asymmetrically in an out-of-plane distortion upon binding of $La(OTf)_3$ and $Lu(OTf)_3$ to accommodate the bound triflate counteranions (ω_{crown} = 0.194 and 0.585). In both the structure of these adducts, the crown is "pushed" by the two triflates binding to the trivalent cation on the same side toward the opposite face of the crown on which only a single triflate is bound. However, this "push" of the polyether chain toward the opposite face in turn encourages the lone triflate on that opposite face to push into the secondary coordination sphere of the nickel center. As a consequence, the trivalent cations appear to uniquely engender enhanced steric crowding in the secondary coordination sphere of the nickel centers in **[Ni,La]** and **[Ni,Lu]**.

With these observations in mind, the specific properties of the Ni(II)/Ni(I) redox manifold in its particular structural context became the focus of our analysis. In particular, we hypothesized

that the attenuated electron transfer rate, k^0, could be attributable to a change in the reorganization energy (λ) associated with interconversion of the Ni(II) and Ni(I) species that together make up the redox manifold under investigation here. In studies of the electron transfer behavior of inorganic complexes, λ is conventionally discussed to include both an inner-sphere component corresponding to reorganization of metal-ligand bonds (bond length changes) upon reduction[44] and an outer-sphere component corresponding to solvation changes upon reduction.[45,46] As we have carried out molecular electrochemical studies of the **[Ni,M]** series here, the electrode itself can thus be considered to undergo virtually no reorganization upon transferring electrons to/from the complexes; any contribution from the solid electrode itself can be ruled out as contributing to the measured heterogeneous electron transfer kinetics.[47,48] On the basis of the striking similarity of the inner-sphere nickel-ligand bond distances for all the heterobimetallic species, the inner-sphere contribution to the reorganization energy (λ) could also be anticipated to be similar for all the complexes.

However, on the basis of the preceding structural observations, the outer-sphere contributions to the reorganization energy (λ_{outer}) cannot be anticipated to be similar for all the complexes. The intrusion of the triflate counteranions into the secondary coordination environment of the redox-active nickel centers in the cases of **[Ni,La]** and **[Ni,Lu]** in particular attracted our attention, as the movement of triflate S–O and/or C–F moieties into this region could have the effect, in solution, of displacing nearby acetonitrile solvent molecules and/or equivalents of tetrabutylammonium and hexafluorophosphate present in the supporting electrolyte. On the one hand, the data available suggest that the λ_{outer} is increased in the case of **[Ni,La]** and **[Ni,Lu]** and thus the energy penalty for reorganizing the triflate moieties that impinge upon the nickel environment appears greater than that associated with solvent and/or electrolyte. This is sensible

considering the greater degrees of freedom associated with uncoordinated solvent molecules and/or electrolyte ions; the triflates, being bound to the trivalent cations, are more tightly associated with the heterobimetallic species in the starting nickel(II) complexes through ionic bonding. Structural rearrangement of the triflates could be more costly than reorganization of the nearby solvent dielectric environment.

We anticipated that the presence of the chemically inert and highly covalent C–F bonds of the triflate anions in the secondary coordination sphere of nickel could drive increases in λ_{outer}. We anticipated that this is the case because of analogous studies in which it is has been recognized that λ_{outer} increases when the solvent polarity is decreased due increase in overall reorganization energy.[49] For example, studies of molecular donor-acceptor pairs with controlled driving forces for electron transfer demonstrated that increased solvent reorganization penalties were associated with lower dielectric solvents less able to stabilize charged species resulting from electron transfer events.[50] Similarly, some of the famous early work exploring experimental proof for the Marcus theory of electron transfer utilized increased solvent polarity to decrease the barrier to electron transfer,[51] enabling observation of the long-postulated inverted kinetics.[52] Considering these observations from prior work, we anticipated that evidence in support of the hypothesis that disruption of the secondary coordination sphere about the nickel centers in the **[Ni,M]** series of complexes could be obtained by a quantitative measure of the degree of disruption of the spatial microenvironment about the redox-active metal.

Quantification of the cation-dependent change in the environment about the nickel centers was carried out using Cavallo's SambVca webtool.[53,54] In particular, we used the webtool to generate topographical steric maps and calculate the percent buried volume ($\%V_b$) about the nickel metal centers in the complexes. As all but one of the prepared heterobimetallic complexes

were characterized by single-crystal XRD, this data could be used to understand the filling of space about the nickel centers with steric bulk from atoms associated with triflates or the macrocyclic ligand. Inspection of the resulting topographical maps (see Figure 10 and pp. S89-S92) shows that the nickel centers (placed at the 0,0 position in the x,y plane) are more open for **[Ni]** and the derivatives incorporating mono- and divalent cations. Looking along the axial direction, space is noticeably filled by atoms associated with bound triflates as well as a single methyl group from the 1,1-dimethyl-1,2-ethylenediamine-derived ligand backbone in each case that extends into the "upper" hemisphere (in the +z direction set in SambVca as shown in Figure 10 and Figure S129). Steric crowding is also present in the "lower" hemisphere (see Figure S130), but has a more negligible contribution from the other ligand backbone methyl group, as it is oriented essentially outward, away from the nickel metal center in each case. In agreement with the qualitative picture that emerged from consideration of interatomic distances from structural data, **[Ni,La]** and **[Ni,Lu]** are the two complexes that feature the most triflate-derived steric congestion about their corresponding nickel centers.

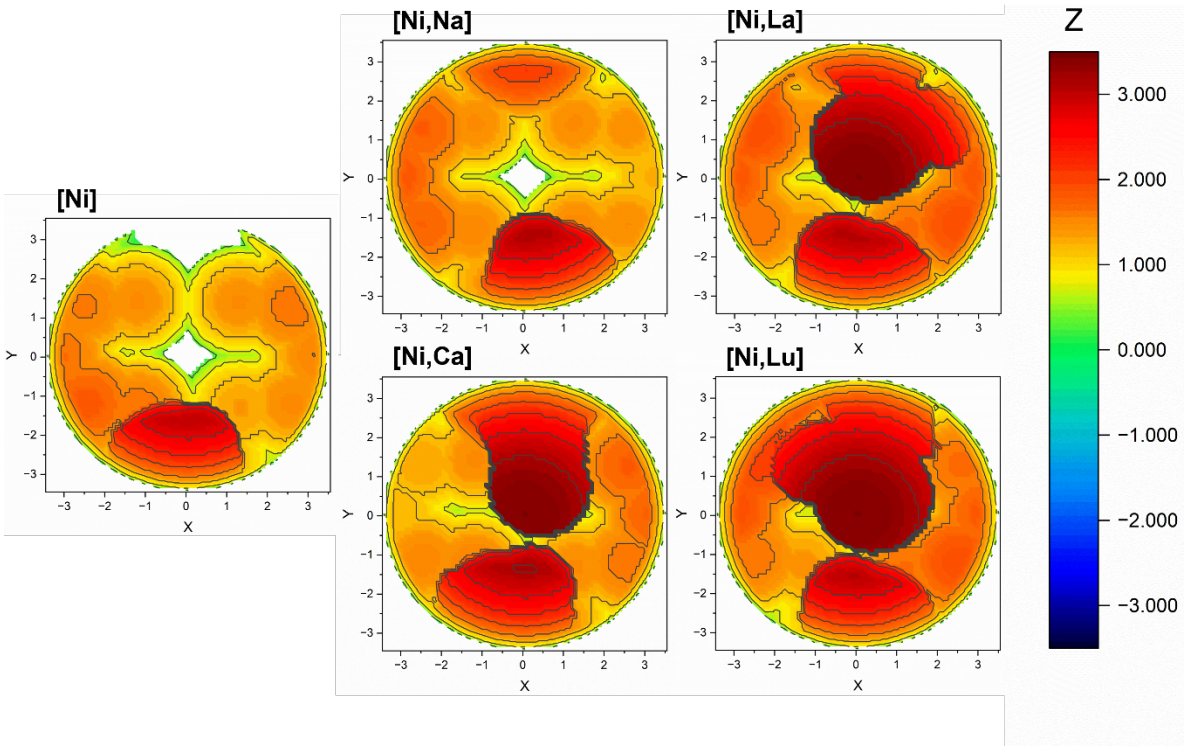

Figure 10. Set of topographic buried-volume plots of monomeric **[Ni]**, **[Ni,Na]**, **[Ni,Sr]**, **[Ni,La]**, and **[Ni,Lu]**. The topographical analysis was carried out with unscaled Bondi radii (1x values) and explicit hydrogen atoms from XRD included. (See Figure S138, Table S6, and pp. S97-S100 for details).

Determination of the overall percent buried volume ($\%V_b$), and the related analogous percent free volume ($\%V_f$; $\%V_f = 1 - \%V_b$) with SambVca afforded a descriptor to parametrize the influence of the trivalent cation salts on the microenvironment about the nickel centers. We plotted the k^0 values as a function of $\%V_f$ to examine for a quantitative correlation between these parameters. As shown in Figure 11, there is a clear relationship in the data, with the highest electron transfer rates being associated with the adducts of mono- and divalent cations, and slower rates associated with the adducts of trivalent cations. However, the diminishment of the

electron transfer rate for **[Ni,La]** is clearly less significant than for **[Ni,Lu]**, and simultaneously, the percent free volume is smaller for **[Ni,Lu]** than **[Ni,La]**. This correlation suggests that the impingement of the triflate counteranions into the microenvironment of the nickel center, along with related structural changes in the macrocyclic ligand driven by the association of the triflate salts of the trivalent cations, result in the diminished electron transfer rate for these species. The correlation shown in Figure 11 is thus in agreement with our hypothesis that occupation of the nickel secondary coordination sphere results in the slower electron transfer kinetics. A greater energy penalty is associated with reorganization of the nickel and its environment upon reduction when trivalent cations are bound in the crown-ether-like site of $\mathbf{L}_{\mathbf{salmen}}$ and their triflate counteranions are located nearby.

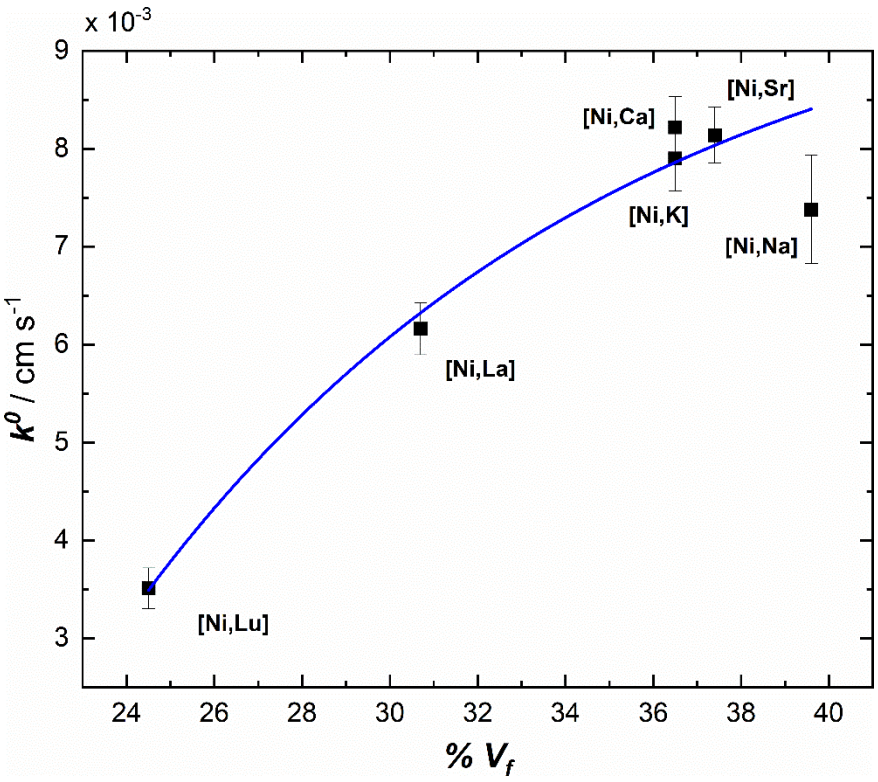

Figure 11. Scatter plot showing the relationship between $\%V_f$ and k^0 of each relevant compound in the **[Ni,M]** family. The blue line is an exponential decay function and is intended primarily to guide the eye.

As presented above, **[Ni,K]** exists in the solid state as a dimer composed of two of the as-synthesized heterobimetallic species. All evidence suggests that the association between the heterobimetallic species is weak, meaning that the complex behaves as a free monomeric **[Ni,K]** species in solution. To provide support for this conclusion in the context of the SambVca analysis and consideration of electron transfer rates, we carried out a buried volume determination with SambVca using the coordinates of the full dimeric species found in the solid states. The results show, as expected, that the percent free volume ($\%V_f$) is much lower in the

case of the dimeric species than the monomer (23.4% vs. 36.5%, respectively; see Figures S135 and S136 for full comparison of data). When the $\%V_f$ of the dimeric **[Ni,K]** complex is used as the descriptor for electron transfer rate (k^0), the behavior does not obey the trend followed by all six other heterobimetallic complexes in this study. Thus, as the interactions holding the dimeric species together in the solid-state can be concluded from the XRD analysis (*vide supra*) to be quite weak, we conclude that **[Ni,K]** does indeed behave as a monomer in solution, but with a modified structure that is different from simply being half of the solid-state dimer (see pp. S59-S60 for details). All of this analysis underscores the sensitivity of buried volume analysis with SambVca to the solid-state structural data and reinforces the conclusion that this tool is useful for interpreting the electron transfer rate data as outlined in this report.

The final piece of evidence from our study which supports the hypothesis that impingement of cation-bound triflate atoms into the nickel secondary coordination sphere results in the slow electron transfer kinetics comes from examining the kinetic data for **[Ni,Y]**. Although no structure from single-crystal XRD is available, we note that the relevant ionic radii of La^{3+} (C.N. = 10), Y^{3+} (C.N. = 9),[5] and Lu^{3+} (C.N. = 9) in our series decrease in this order: 1.27, 1.22, and 1.03 Å.[19] Similarly, the k^0 values from our analysis decrease monotonically in the same order: 6.2±0.3, 3.7±0.2, and 3.5±0.2 cm s^{-1}. From the relationship shown in Figure 2, we could anticipate that incorporation of Y^{3+} would lead to a Ni•••Y separation with a value between those of La^{3+} and Lu^{3+}. Thus, the data for **[Ni,Y]** lie along the same trend as determined from the free volume analysis. The ionic radius value for Y^{3+} is intermediate between La^{3+} and Lu^{3+} and the k^0 value is also intermediate (see Figure S139). We thus conclude that a decrease in solvent/electrolyte-exposed free volume correlates quantitatively with diminished electron transfer rates for the adducts of the triflate salts of the trivalent cations.

DISCUSSION

In planning the studies described here, we hoped that the use of a non-conjugated diimine backbone to assemble heterobimetallic nickel complexes would enable observation of a reversible redox wave in electrochemical studies and detailed studies of the associated complexes. Gratifyingly, we found that this strategy was successful across complexes incorporating a full range of mono-, di-, and trivalent secondary metal cations. Importantly, our observations of rather negative reduction potentials for these complexes and the observation of chemically reversible processes were precedented in a number of prior studies of monometallic and multimetallic complexes, but to the best of our knowledge, the studies reported here are the first to include study of trivalent cation adducts. Moreover, through the EPR studies described here, we were able to rigorously assign the observed redox waves as being associated with nickel(II)/nickel(I) interconversion, rather than ligand-centered reduction which can be a concern in systems (like ours) which feature conjugated ligand backbone components.[33]

With regard to the confirmation of generation of paramagnetic nickel(I) species, the results reported here represent an appealing counterpoint to findings that we have also recently reported elsewhere[8] on the properties of paramagnetic oxovanadium(IV) (i.e., vanadyl, $[VO]^{2+}$) complexes supported by $\mathbf{L}_{\mathbf{salmen}}$, which was also utilized here. In the prior report, room-temperature EPR spectra (coupled with spectral simulations) revealed linear correlations of both the ^{51}V (ca. 99.8% abundant $I = 7/2$) isotropic hyperfine coupling constants (A_{iso}) and average g-values with the Lewis acidities of the incorporated secondary metal cations, as judged by the pK_a values of the corresponding aqua complexes. In the context of established work in the field on correlations of ligand donor strength with these EPR parameters,[55] we were able to provide spectroscopic evidence that supports the hypothesis that incorporation of metal cations to form heterobimetallic

complexes of the type explored here results in diminished electron donation from the bridging phenoxide moieties to the core metal center.[56] The EPR spectral data reported here, however, do not show a correlation between any of the extracted EPR parameters and the pK_a measure of Lewis acidity. This suggests that the magnetic properties of the nickel(I) complexes are less sensitive to heterometallic effects, although we note that as nickel lacks an abundant naturally-occurring isotope with nonzero nuclear spin (^{61}Ni has I = 3/2 but this isotope represents only 1.1% of natural nickel), any hyperfine effects would be difficult to measure in these systems. We had anticipated that diminished covalency between the bridging phenoxide ligands and the nickel metal center could result in greater s-character in the radical species and give rise to higher g-values, as would be implied from the corresponding results in the vanadyl system, but there is no substantial evidence for this effect at this time. On the other hand, there is evidence that the first coordination spheres of the nickel(II) centers are very similar across our family of complexes (*vide infra*); this could contribute to the more minor variations across the measured EPR parameters of the nickel(I) species in this work. At least, the current results highlight that the vanadyl moiety is a uniquely useful spectroscopic probe for use in EPR studies, as has been highlighted previously.[57]

The topological maps and buried volume analysis carried out with the SambVca webtool provided quantitative data that demonstrate that the impingement of the triflate counteranions associated with the trivalent cations into the secondary coordination sphere of the nickel center results in diminished electron transfer rates. SambVca has emerged as a broadly useful tool in structural studies of inorganic and organometallic systems, as it offers the ability to generate the maps and quantitative buried volume analyses from the Cartesian coordinates available from single-crystal XRD analysis or computational studies.[53] Our use of SambVca for this study was

inspired by the use of the webtool, in particular, for applications in catalysis, where it has been applied to understand how substrates might approach metal centers to undergo catalyzed reactions.[53,58] We note here that although we are aware of use of SambVca for applications in design of ligands for catalysis and correlations of product yields with steric parameters,[2,59] we are not aware of any prior study which was able to use steric data from the topological mapping to quantify and elucidate the structural origin of measured electron transfer kinetics. We anticipate, first, that this approach could be useful in other studies of multimetallic complexes, because electron transfer behavior is an important determinant of the usefulness of many such complexes. Significant work from recent years has focused on development of multimetallic catalysts and materials which rely on electron transfer events to accomplish their designated functions; for example, multimetallic species have emerged as appealing catalysts for oxidation reactions,[60] model complexes for enzyme active sites,[3,61] and motifs for influencing the structural[62] and redox properties of the actinides.[8,63]

Along the line of this latter point, Fukuzumi and co-workers presented one particularly relevant and beautiful study[4] of how incorporation of secondary metal cations could be used to modulate the driving force for electron transfer in an oxygen-powered system for C–H bond functionalization; in their system, the kinetics of electron transfer (and by extension, reaction turnover) were governed by the reduction potential of a key heterobimetallic species which underwent chemical reduction by an exogeneous equivalent of decamethylferrocene to trigger reactivity. Here, rather than using secondary metal cations to modulate the driving force for electron transfer, we have found a role for the secondary metal cations in governing the reorganization energy associated with a particular redox manifold. The mechanism underlying a role for secondary cations in driving increased reorganization energy penalties was not explicitly

described in the work of Fukuzumi and co-workers, but the appearance of some of the data in these authors' report suggests that such an effect could also be operative in their system. Specifically, points on their Marcus-like curve of reaction kinetics versus estimated thermodynamic driving force for the key reduction reaction show that the reorganization energy for trivalent cation adducts was apparently greater by about 340 meV compared to the value associated with mono- and divalent adducts (2.66 vs. 2.32 eV).[4] Although this difference was not explained in the noted publication, we feel that our results here offer a preliminary explanation for the origin of such an effect. The authors utilized triflate salts in their work, as we have here as well in light of their useful solubility in acetonitrile and other polar organic solvents, and thus there could be a unique tendency for triflate salts to engender these effects. Exploration of counteranion-dependent behavior is thus underway in our laboratory at this time to make progress on understanding these effects in greater detail.

As atomic coordinates from XRD were used as the input for the SambVca analysis, we were able to examine the individual influences of the chemical moieties in the heterobimetallic complexes that give rise to the changes in free volume about the nickel centers across the series studied here (see Table S5). The "upper" methyl groups on the di-imine bridge of the macrocyclic ligand contribute only 2-3% of the buried volume for all of the nickel species studied here. This is consistent with the apparent rigidity of the immediate environment about the Ni center in the plane of the Schiff base ligand. On the other hand, the impact of the triflate counteranions varies markedly across the series, with the greatest influence arising in **[Ni,Lu]** and **[Ni,La]**. Examining these complexes in detail reveals that this effect is greater for small Lu^{3+} due to the out-of-plane distortion induced in the crown (quantified as described above by the ω_{crown} parameter) that forces two triflates toward the nickel center. This is driven by a notable

bowing of the macrocyclic ligand that is visible to the eye in the XRD structure of **[Ni,Lu]** (see Figure 1). Thus, despite the macrocyclic deformation, removal of the methyl groups from the di-imine bridge would not make a substantial difference in the steric congestion about the nickel site.

We utilized a similar range of triflate salts of secondary metal cations in our prior study of the ligand-centered reduction of macrocyclic palladium(II) complexes assembled with the $\mathbf{L}_{\mathbf{salmen}}$ ligand.[9] In that work, we measured a correlation between the Lewis acidity (pK_a value) associated with the secondary cations and electrochemically-measured reorganization energy, with the more Lewis acidic cations being associated with greater reorganization energies. At that time, we speculated that changes in ligand structure and/or contributions from follow-up chemical reactivity might induce this trend in the data, but we did not have conclusive evidence to support these concepts. Returning to the structural data from single-crystal XRD analysis associated with our prior report,[9] we used SambVca to generate topographical maps and buried volume data for the **[Pd,M]** series of complexes. As in the approach taken in the new work here with the **[Ni,M]** series, we set the Pd center in each complex as the geometric origin (x,y = 0,0) for analysis. However, we anticipated that, as the Pd center was not the localized atom/center undergoing reduction, the same effect of steric congestion induced by triflate placement resulting from the trivalent-cation binding might not be apparent. However, the greatest measured reorganization energies were again associated with the trivalent cation adducts (see Figure 12). This is attributable, in our view, to the location of palladium being near the presumably redox-active conjugated fragments within the $\mathbf{L}^{\mathbf{salmen}}$ ligand backbone. Additionally, the adduct with the greatest estimated reorganization energy (slowest apparent ET kinetics) was the **[Pd,Lu]** complex, followed by **[Pd,Y]** with slightly lower reorganization energy (faster ET kinetics). This

trend and the measurement of modest reorganization energy values for the other palladium complexes in that study suggest that impingement of the triflates into the secondary coordination sphere of the conjugated portion of the $\mathbf{L}_{\mathbf{salmen}}$ backbone undergoing reduction results in the slow ET in that system as it does for our **[Ni,M]** series of complexes. Coincidentally, the conjugated system within the greater $\mathbf{L}_{\mathbf{salmen}}$ platform is located near the Schiff-base site, meaning that the triflates are located near to both the redox-active ligand system in the palladium case and the redox-active nickel center in the case reported here. All of these findings provide additional support for the model developed here to explain the modulation of electron transfer kinetics.

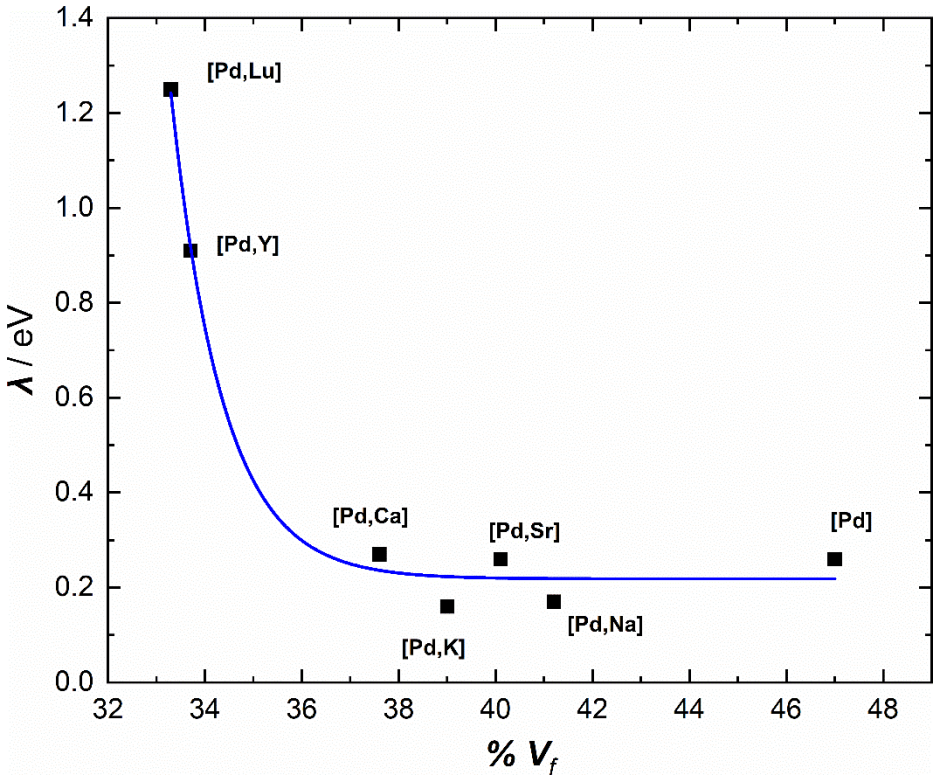

Figure 12. Scatter plot showing the relationship between λ and $\%V_f$ for the previously studied **[Pd,M]** family. The blue line is an exponential growth function and is intended primarily to guide the eye.

In the studies of both the **[Ni,M]** and **[Pd,M]** complexes, the first coordination spheres of the Group 10 metal cores of the complexes do not show significant structural perturbations upon incorporation of the secondary metal cations. This observation applies to the tight range of Ni–O_{phen} and Ni–N_{imine} distances (see Figures S114 and S118) in the **[Ni,M]** series, as well as the uniformly low values of the τ_4 geometry index for **[Ni]** and all the heterobimetallic complexes. Our prior report shows that the noted parameters are rather invariant across the **[Pd,M]** series as well. Contrasting with this behavior for Ni(II) and Pd(II), the structural properties of the vanadyl (VO^{2+}) complexes of the $\mathbf{L_{salmen}}$ ligand vary more dramatically across a series containing the monometallic complex and the Na^+ and Ca^{2+} adducts; the V–O_{phen} distances were elongated while the V–O_{oxo} distances were contracted along the series **[VO]** – **[VO,Na]** – **[VO,Ca]**. We anticipate that these disparate findings may be attributable partially to the greater (structural) degrees of freedom associated with the vanadyl complexes; the vanadium center sits above the plane of the macrocyclic ligand, owing to its square pyramidal geometry, and compensation for diminished phenoxide donor power can apparently come from enhanced donation from the oxo group. Here, the nickel stays firmly in its square-planar geometry and bond distances do not change; this rigidity is a hallmark of the **[Ni,M]** series and its covalent Ni–L bonds, and we anticipate at this stage that it could lead to the charge-dependent electrochemical data shown in Figure 7. Investigation of the structures of the reduced species could shed light on the question of whether this apparent structural rigidity is translated to any significant degree to the nickel(I) forms of the complexes.

In our recent work with a family of cerium(III) complexes, we identified that cation-cation repulsion across heterometallic cores should be considered when interpreting the behavior of heterobimetallic complexes that feature bridging ligands.[38] Cation-cation repulsion of a

Coulombic nature was observable in that work between Ce^{3+} and $\mathbf{M}^{n+}$ centers, a feature that we have attributed to the consideration that the electrostatic interactions which influence pK_a values involve $\mathbf{M}^{n+}$ complexes of neutral H_2O or monoanionic hydroxide only, rather than multiple metal centers with intrinsic positive charges. In the case of the work here with the **[Ni,M]** complexes, this cation-cation repulsion does not appear to be as significant, likely because of the expected strong(er) Ni–$O_{phenoxide}$ bonding. The results of a deconvolution analysis (see p. S84) aimed at examining the approach of the secondary cations to the square-planar covalent nickel core suggest that cation-cation repulsion only mildly affects interpretation of data in this system as a function of the pK_a values. In particular, the distance defined as "a" in our analysis (between the centroid of O1 and O2 and the nickel metal center; see Figure S122) suggest that cation-cation repulsion could play a role in slight elongation of the distance when stronger Lewis acids approach the nickel center, resulting in enhanced repulsion and thus deviation from linear dependence on Lewis acidity. Similar analysis using ratios of the charge and ionic radii values for the secondary cations return related plots that confirm the presence of vestiges of cation-cation repulsion in structural examination of Lewis acidity driven effects (see Figures S125 and S126). The conceptually related anion-anion repulsion between the phenoxide O atoms (O1 and O2) is apparently minimized however, as plots of this distance vs. the ionic radii of the secondary cations confirm a strong nonlinear correlation (see Figure S120) in accord with a tightening of the O1–Ni–O2 angle (defined as θ; see Figure S124). Examination of the O1•••O2 distance as a function of pK_a (see Figure S121) returns a corresponding plot for all of these; the smaller cations in each case are associated with smaller than predicted interatomic separations; this can be attributed to the effect of cation-anion attraction between the highly Lewis acidic cations and the anionic phenoxide groups themselves. Considering all of these features, we

anticipate that the successful interpretation of "Lewis acid" dependent tuning effects with pK_a values is a result of the recognized correlations between pK_a values and a given cation's charge, radius, and electronegativity as outlined by Wulfsburg.[18]

Considering the importance of charge in these systems, it is valuable to consider the structural consequences of generation of the Ni(I) oxidation state in our family of complexes. As Ni(I) should be larger than Ni(II), if the O and N atoms of the salen-like [N_2,O_2] core are constrained to have a more or less fixed separation (sensible considering the macrocyclic nature of our complexes), the Ni center could be predicted to move out of the plane containing the [N_2,O_2] core. This could cause the macrocycle to open up across the O1•••O2 separation that is a shared polyhedral edge with the secondary metal cations. Opening of this edge could induce considerable ligand movement, and in the case of the trivalent cations, there are three triflates that could move instead of the one or two in the adducts of monovalent or divalent cations. As any rearrangement in the trivalent cations' coordination spheres markedly affects %$V_{f,}$ it could be anticipated that the Ni(I) adducts of the trivalent cations could have significant redox-induced structural deformations that would drive diminished electron transfer kinetics through increased reorganization penalties. Additionally, we previously noted contacts between the Ni centers and nearby triflate-derived O and F atoms above and below the macrocyclic plane for the trivalent adducts; for **[Ni,Lu]**, O23 and F13 are located, respectively, 2.908(6) and 3.054(7) Å away from Ni, while for **[Ni,La]**, atoms F32 and O23′ are located, respectively, 3.30(1) and 3.70(3) Å away from Ni. Ni(I) could be more likely to interact with these atoms than Ni(II) upon formation.

Considering the importance of the impingement of the triflate-derived S–O and C–F moieties into the microenvironment of the nickel centers in these complexes, it is also valuable to consider the result that would be obtained in our systems with simpler tetrahedral monoanions or dianions

like perchlorate, sulfate, or phosphate in place of triflate. We anticipate that these anions, as less sterically demanding species, would impinge to a lesser extent into the nickel microenvironment. Fewer anions would be required to neutralize charge if divalent or trivalent anions were used, and this would also result in decreased impingement into the nickel microenvironment. Thus, if faster electron transfer is required in trivalent adducts, substitution of triflate for another, smaller and/or highly charged anion could be valuable. The formation of sterically congested coordination spheres about the secondary metal cations is, as we have shown, driven partially by use of the triflate counteranions; this is supported by the structures from XRD, in that none show bound solvent, implying that triflates prefer to bind to the metal cations and to adopt bidentate configurations when space on the cations' coordination spheres remains, excluding solvent binding completely. Plotting the measured values of k^0 vs. ionic radius (see Figure S139) confirms this is the case, as the rates of electron transfer for the divalent and trivalent secondary metals having coordination numbers greater than or equal to nine and featuring two or more bound triflate counteranions (Sr^{2+}, La^{3+}, Y^{3+}, and Lu^{3+}) are essentially linearly dependent upon the ionic radii values for the secondary cations, echoing the trend in cation position shown in Figure 2. However, **[Ni,K]**, and **[Ni,Sr]**, show fast heterogeneous ET behavior despite the high coordination numbers of the secondary cations because steric crowding about Ni is more modest than in the adducts of trivalent cations. Anion charge, size, and ability to form bridging interactions drive changes in the measured $\%V_{f,}$ about the nickel center and could also be related to formation of the pseudo-octahedral O•••Ni•••F interactions; consequently, triflate appears unique in driving the measured changes in the family of complexes studied here. However, we note that triflate salts were selected for use here due to their high solubility, enabling the

systematic studies reported here and overcoming the very likely limited solubility of less sterically demanding salts featuring counteranions such as perchlorate.

In light of all these observations, use of tailored heteroditopic ligands for binding two or more metal cations can be confidently concluded to aid in the observation of structural and/or behavioral trends driven by exchange of one metal. This could be because ligands of the sort used by our group and others (multidentate chelates or macrocycles) are less flexible and impose restrictions on metal coordination numbers and geometries. In the work presented here, this restrictive nature has been shown to drive impingement of triflate moieties into the secondary coordination sphere of redox-active nickel, as detectable through the structure-dependent diminishment in heterogeneous electron transfer rates. This effect is a clear result of both the demanding properties of the triflate salts of the trivalent cations as well as the structure of the macrocyclic ligand; the ligand drives a lateral movement of the cations and their triflates that depends on ionic radius, thus taking what would conventionally be a three-dimensional electrostatic effect and constraining it into the approximately two-dimensional plane defined by the $\mathbf{L}_{\mathbf{salmen}}$ ligand and along the Ni•••**M** vector. In other words, in these complexes, the [O–Ni–O] group is effectively like a large, rigid, and redox-active carboxyl group and the cationic **M** species, along with their triflate counteranions to some extent, move in and out along the Ni•••M vector depending on their ionic radii values. With this in mind, this work highlights this unique role of macrocyclic ligands in influencing electron transfer behavior, suggesting new opportunities for rational control over electron transfer rates in systems of this type. We anticipate that an appealing direction for future work could be examination of ligand variations that take into account tunable degrees of freedom, an approach that could directly examine the vectorization of cation-induced effects and afford new insights into their parametrization.

CONCLUSION

In this work, we have prepared a family of Ni-based heterobimetallic complexes incorporating mono-, di- and tri-valent secondary metals via a divergent synthetic pathway. These complexes demonstrate reliably tunable and chemically reversible Ni(II)/Ni(I) couples, as confirmed by solution-based cyclic voltammetry and cryogenic X-band EPR spectroscopic experiments. Investigation of the solid-state structures of the heterobimetallic complexes with XRD analysis revealed that the Ni•••**M** distances are driven by the ionic radii of the secondary metal cations and that there is a noticeable increase in the crowding about the Ni(II) ion when trivalent secondary cations are bound; the crowding about Ni(II) is driven by impingement of atoms from the triflate counter-anions bound to the nearby secondary cation. The heterogeneous electron transfer rate to the heterobimetallic complexes is also slowed upon incorporation of the trivalent secondary metal cations, prompting interrogation of the steric environment about the Ni(II) ion with the SambVca webtool. This interrogation enabled visualization of the crowding engendered by the inclusion of the trivalent secondary metal cations into the heterobimetallic complexes, and confirmed a well-defined quantitative relationship between $\%V_f$ and k^0. Re-examination of data from our previous study of analogous **[Pd,M]** complexes revealed a similar relationship between $\%V_f$ and k^0, suggesting that the presence of the triflate counter-anions on the trivalent cations plays an important role in increasing the reorganization energy associated with redox in both systems.

Taken together, the results of this study shed light on the consequences of incorporating trivalent cations into heterobimetallic species, and the important role that these cations' counter-anions can play in influencing the chemical and electrochemical properties of the resulting heterobimetallic adducts. The results suggest that exciting opportunities lie in exploration of the

properties of other salts of the secondary cations, particularly those salts that feature more weakly coordinating counter-anions that could be less likely to closely associated with the bimetallic cores in solution. Such compounds could be anticipated to display faster electron transfer kinetics, a feature sought in most applications, as well as even greater "tuning power" from the incorporated, effectively Lewis acidic secondary metal cations. Investigation of these opportunities is currently underway in our laboratory.

EXPERIMENTAL SECTION

General Considerations. All manipulations were carried out in dry N_2-filled gloveboxes (Vacuum Atmospheres Co., Hawthorne, CA) or under N_2 atmosphere using standard Schlenk techniques unless otherwise noted. All solvents were of commercial grade and dried over activated alumina using a PPT Glass Contour (Nashua, NH) solvent purification system prior to use, and were stored over molecular sieves. All chemicals were purchased from major commercial suppliers and used as received or after extensive drying. 2,3-dihydroxybenzaldehyde was sublimed in vacuo before use. CD_3CN was purchased from Cambridge Isotope Laboratories and dried over 3 Å molecular sieves. ^{1}H, ^{13}C, and ^{19}F NMR spectra were collected on 400 and 500 MHz Bruker spectrometers and referenced to the residual protio-solvent signal in the case of ^{1}H and ^{13}C. ^{19}F NMR spectra were referenced and reported relative to CCl_3F as an external standard following the recommended scale based on ratios of absolute frequencies (Ξ). Chemical shifts (δ) are reported in units of ppm and coupling constants (J) are reported in Hz. NMR spectra are given in the SI (Figures S1 to S39). Electronic absorption spectra were collected with

an Ocean Optics Flame spectrometer, in a 1-cm path length quartz cuvette. Details regarding use of the SambVca 2.1 webtool are given in the Supporting Information (p. S88).

Electrochemistry. Electrochemical experiments were carried out in a N_2-filled glovebox in dry, degassed CH_3CN. 0.10 M tetra(n-butylammonium) hexafluorophosphate ($[nBu_4N]+[PF_6]–$); Sigma-Aldrich, electrochemical grade) served as the supporting electrolyte. Measurements were made with a Gamry Reference 600+ Potentiostat/Galvanostat using a standard three-electrode configuration. The working electrode was the basal plane of highly oriented pyrolytic graphite (HOPG) (GraphiteStore.com, Buffalo Grove, Ill.; surface area: 0.09 cm^2), the counter electrode was a platinum wire (Kurt J. Lesker, Jefferson Hills, PA; 99.99%, 0.5 mm diameter), and a silver wire immersed in electrolyte served as a pseudoreference electrode (CH Instruments). The reference was separated from the working solution by a Vycor frit (Bioanalytical Systems, Inc.). Ferrocene (Sigma Aldrich; twice-sublimed) was added to the electrolyte solution prior to the beginning of each experiment; the midpoint potential of the ferrocenium/ferrocene couple (denoted as $Fc^{+/0}$) served as an internal standard for comparison of the recorded potentials. Concentrations of analyte for cyclic voltammetry were ca. 2 mM unless otherwise noted. Compensation for solution resistance (measured by impedance spectroscopy to be small, ca. 110–150 Ω) was not carried out for any of the data presented here; based on preliminary comparisons, the data quality was higher without applying compensation.

Synthesis and characterization

Synthesis of 3,3'-(3,6-Dioxaoctane-1,8-diyldioxy)bis(2-hydroxybenzaldehyde). Under an inert atmosphere of nitrogen, a dry Schlenk flask was loaded with 2,3-dihydroxybenzaldehyde (1.2 g, 8.85 mmol) dissolved in 15 mL of dry THF. This solution was transferred using a syringe

to a suspension of NaH (0.47 g, 19.5 mmol) in 5 mL of dry THF under N_2 over a period of 1 hour. The temperature was kept below 25 °C. The color change to bright yellow indicates the formation of disodium salt of 2,3-dihydroxybenzaldehyde. The ice bath was removed after addition and the mixture was stirred for 1 hour at room temperature. Under a positive flow of N_2, triethylene glycol ditosylate (2.03 g, 4.42 mmol) dissolved in 25 mL of dry THF was added to the yellow mixture in a single aliquot using a syringe. The resulting mixture was then stirred for 60 hours under static N_2 atmosphere and 45 °C. Addition of 80 mL of water resulted in a dark brown solution that was extracted twice with $CHCl_3$. The aqueous layer was treated with 6 M HCl until the pH of the mixture was 1. This mixture was then extracted with three portions of $CHCl_3$. The combined organic layers were washed with 1 M HCl and dried over anhydrous $MgSO_4$. Evaporation of solvent yielded a pale-yellow solid which was used without any further purification. Yield: 84% (1.46 g). Spectroscopic characterization by ^{1}H NMR matches spectra obtained in a prior report.[21]

Synthesis of [Ni,Ba]. To a three-necked flask of a refluxing solution of Ba(OTf)2 (1.64 g, 3.78 mmol) dissolved in 250 mL of CH_3OH (0.015 M), 1 equiv. of 3,3'-(3,6-Dioxaoctane-1,8-diyldioxy)bis(2-hydroxybenzaldehyde) (1.46 g, 3.73 mmol) in 65 mL THF (0.06 M) was slowly added. 1 equiv. of 1,2-diamino-2-methylpropane (0.336 g, 3.81 mmol) in 65 mL CH_3OH (0.059 M) was added dropwise over a period of 5 hours. The reaction mixture was refluxed for 30 minutes. 1 equiv. of $Ni(OAc)_2$*4(H_2O) (0.94 g, 3.77 mmol) was added, and the solution was allowed to reflux for 10 more minutes before being left to cool to room temperature overnight. The solution was then evaporated on the rotary evaporator until concentrated. Ether was used to wash and terterate the solution and resulting solid until a brown powder formed. Spectroscopic characterization by ^{1}H NMR is in agreement with spectra obtained in a prior report.[21]

Synthesis of [Ni]. An excess of guanidinium sulfate (4.06 g, 18.6 mmol) dissolved in 250 mL water was added to a suspension of **[Ni,Ba]** (1.16 g, 1.24 mmol) in 50 mL $CHCl_3$ under stirring for at least four days. The organic layer was separated, and the water layer was washed with $CHCl_3$ twice or until the $CHCl_3$ was clear. The $CHCl_3$ that contains the product is then dried on a rotary evaporator until concentrated. The concentrated solution is then washed with cold hexanes to precipitate the product in the form of a brown, fine powder. This powder is then collected by vacuum filtering the solution with a medium frit. Spectroscopic characterization by ^{1}H NMR confirmed the expected structure in agreement with a prior literature report.[21]

[Ni]. Yield: 84.4%. ^{1}H NMR (500 MHz, CD_3CN) δ (ppm): 7.60 (s, 1H, *H3*), 7.59 (s, 1H, *H3*), 6.88 (d, $^3J_{H,H}$ =8.05, 1H, *H4*), 6.81 (d, $^3J_{H,H}$ =8.00, 1H, *H4*), 6.71 (d, $^3J_{H,H}$ =7.50, 2H, *H6*), 6.46 (t, $^3J_{H,H}$ =7.10, 1H, *H5*), 6.45 (t, $^3J_{H,H}$ =7.55, 1H, *H5*), 3.95 (m, 4H, *H7*), 3.72 (m, 4H, *H8*), 3.65 (s, 4H, *H9*), 3.24 (s, 2H, *H2*), 1.46 (s, 6H, *H1*). ^{13}C {^{1}H} NMR (126 MHz, CD_3CN) δ (ppm): 163.29, 160.20, 156.80, 156.15, 151.33, 151.23, 125.27, 124.69, 121.47, 121.27, 114.60, 114.58, 113.75, 113.71, 71.58, 70.48, 69.60, 67.94, 67.92, 66.71, 25.88. Cyclic Voltammetry (0.1 M $[nBu_4N]^+[PF_6]^-$ in CH_3CN): $E_{1/2}$ = –2.129 V vs. $Fc^{+/0}$. Electronic absorption spectrum in CH_3CN (M^{-1} cm^{-1}): 420 (5398), 550 (103) nm.

Synthesis of [Ni,M] heterobimetallic complexes. Under an inert atmosphere, a heterogeneous solution of **[Ni]** in CH_3CN was added to 1 equiv. of corresponding metal salt solution in CH_3CN and stirred for 30 minutes. The reaction is accompanied by a color change of the brown solution of **[Ni]** to a red or orange-colored solution, depending on the concentration. The solvent was removed in vacuo to give the desired product. Yields were typically near quantitative (*vide infra*). Crystals suitable for X-ray diffraction were obtained by vapor diffusion of diethyl ether into a CH_3CN solution of the **[Ni,M]** complexes for **[Ni,K]**, **[Ni,Na]**, and **[Ni,Sr]**.

Crystals of **[Ni,Ca]** suitable for X-ray diffraction were obtained by vapor diffusion of CH_2Cl_2 into a CH_3OH solution stored outside the glovebox. Crystals of **[Ni,La]** and **[Ni,Lu]** suitable for X-ray diffraction were obtained by vapor diffusion of CH_2Cl_2 into a CH_3CN solution inside of the glovebox.

Elemental analyses for all bimetallic complexes were performed by Midwest Microlab, Inc. (Indianapolis, IN).

[Ni,K]. Yield: 96%. ^{1}H NMR (500 MHz, CD_3CN) δ (ppm): 7.65 (s, 2H, *H3*), 6.98 (d, $^3J_{H,H}$ =8.05, 1H, *H4*), 6.91 (d, $^3J_{H,H}$ =8.00, 1H, *H4*), 6.85 (d, $^3J_{H,H}$ =7.70, 2H, *H6*), 6.59 (t, $^3J_{H,H}$ =7.65, 1H, *H5*), 6.58 (t, $^3J_{H,H}$ =7.55, 1H, *H5*), 4.06 (m, 4H, *H7*), 3.83 (m, 4H, *H8*), 3.73 (s, 4H, *H9*), 3.28 (s, 2H, *H2*), 1.48 (s, 6H, *H1*). ^{13}C {^{1}H} NMR (126 MHz, CD_3CN) δ (ppm): 164.17, 161.09, 154.58, 153.93, 150.19, 150.09, 126.24, 125.67, 121.51, 121.33, 115.85, 115.82, 114.43, 71.50, 70.29, 70.27, 69.13, 67.77, 67.34, 25.76. ^{19}F NMR (471 MHz, CD_3CN) δ –80.19. Anal. Calcd. for $C_{25}H_{28}F_3KN_2O_9SNi$ ([Ni,K]): C 43.68, H 4.08, N 4.11; Found: C 43.37, H 4.28, N 4.07. Cyclic Voltammetry (0.1 M $[nBu_4N]^+[PF_6]^-$ in CH_3CN): $E_{1/2}$ = –1.949 V vs. $Fc^{+/0}$. Electronic absorption spectrum in CH_3CN (M^{-1} cm^{-1}): 409(4323), 545 (104) nm.

[Ni,Na]. Yield: 98%. 1H NMR (500 MHz, CD_3CN) δ (ppm): 7.69 (s, 2H, *H3*), 7.00 (d, $^3J_{H,H}$ =8.05, 1H, *H4*), 6.93 (d, $^3J_{H,H}$ =8.00, 1H, *H4*), 6.88 (d, $^3J_{H,H}$ =7.75, 2H, *H6*), 6.61 (t, $^3J_{H,H}$ =7.80, 1H, *H5*), 6.60 (t, $^3J_{H,H}$ =7.70, 1H, *H5*), 4.06 (m, 4H, *H7*), 3.82 (m, 4H, *H8*), 3.70 (s, 4H, *H9*), 3.32 (s, 2H, *H2*), 1.48 (s, 6H, *H1*). ^{13}C {^{1}H} NMR (126 MHz, CD_3CN) δ (ppm): 163.73, 160.71, 153.83, 153.19, 149.54, 149.43, 125.74, 125.19, 120.99, 120.80, 115.60, 115.57, 114.37, 114.35, 70.93, 69.54, 69.51, 68.16, 67.44, 66.91, 25.36. ^{19}F NMR (376 MHz, CD_3CN) δ –80.19. Anal. Calcd. for $C_{25}H_{28}F_3NaN_2O_9SNi$ (**[Ni,Na]**): C 44.73, H 4.20, N 4.17; Found: C 43.97, H 4.38, N

4.45. Calcd for $C_{25}H_{28}F_3NaN_2O_9SNi$ + 0.5 H_2O: C 43.56, H 4.39, N 4.06. Water inclusion in the sample likely resulted from shipping, as these complexes are hygroscopic. Cyclic Voltammetry (0.1 M $[nBu_4N]^+[PF_6]^-$ in CH_3CN): $E_{1/2}$ = –1.953 V vs. $Fc^{+/0}$. Electronic absorption spectrum in CH_3CN (M^{-1} cm^{-1}): 406(4690), 549 (92) nm.

[Ni,Sr]. Yield: 98%. ^1H NMR (500 MHz, CD_3CN) δ (ppm): 7.72 (s, 1H, *H3*), 7.71 (s, 1H, *H3*), 7.14 (d, $^3J_{H,H}$ =8.00, 1H, *H4*), 7.06 (d, $^3J_{H,H}$ =6.15, 1H, *H4*), 7.04 (d, $^3J_{H,H}$ =7.00, 2H, *H6*), 6.77 (t, $^3J_{H,H}$ =7.95, 1H, *H5*), 6.76 (t, $^3J_{H,H}$ =7.95, 1H, *H5*), 4.25 (m, 4H, *H7*), 4.04 (m, 4H, *H8*), 3.90 (s, 4H, *H9*), 3.35 (s, 2H, *H2*), 1.51 (s, 6H, *H1*). ^{13}C {^1H} NMR (126 MHz, CD_3CN) δ (ppm): 165.19, 162.05, 151.28, 150.62, 148.95, 148.82, 127.51, 126.96, 121.34, 121.16, 117.74, 117.71, 115.78, 71.31, 70.93, 70.88, 69.20, 68.03, 25.57. ^{19}F NMR (471 MHz, CD_3CN) δ –80.09. Anal. Calcd. for $C_{26}H_{28}F_6SrN_2O_{12}S_2Ni$ (**[Ni,Sr]**): C 35.29, H 3.19, N 3.16; Found: C 34.41, H 3.36, N 3.09. Calcd. For $C_{26}H_{28}F_6SrN_2O_{12}S_2Ni$ + H_2O: C 34.58, H 3.35, N 3.10. Water inclusion in the sample is due to the hygroscopic nature of the complex, as water is retained in the ^1H-NMR even after overnight drying of the complex. Cyclic Voltammetry (0.1 M $[nBu_4N]^+[PF_6]^-$ in CH_3CN): $E_{1/2}$ = –1.684 V vs. $Fc^{+/0}$. Electronic absorption spectrum in CH_3CN (M^{-1} cm^{-1}): 390 (4521), 540 (114) nm.

[Ni,Ca]. Yield: 96%. 1H NMR (500 MHz, CD_3CN) δ (ppm): 7.74 (s, 1H, *H3*), 7.73 (s, 1H, *H3*), 7.15 (d, $^3J_{H,H}$ =8.00, 1H, *H4*), 7.07 (d, $^3J_{H,H}$ =8.00, 1H, *H4*), 7.05 (d, $^3J_{H,H}$ =7.85, 2H, *H6*), 6.79 (t, $^3J_{H,H}$ =7.95, 1H, *H5*), 6.78 (t, $^3J_{H,H}$ =7.90, 1H, *H5*), 4.25 (m, 4H, *H7*), 4.06 (m, 4H, *H8*), 3.94 (s, 4H, *H9*), 3.36 (s, 2H, *H2*), 1.52 (s, 6H, *H1*). ^{13}C {^1H} NMR (126 MHz, CD_3CN) δ (ppm): 165.05, 161.88, 150.65, 150.05, 148.69, 148.59, 127.35, 126.80, 121.17, 120.96, 117.98, 117.95, 115.86, 115.79, 71.07, 70.40, 68.63, 68.14, 68.03, 67.99, 25.53. ^{19}F NMR (471 MHz, CD_3CN) δ –80.14. Anal. Calcd. for $C_{26}H_{28}F_6CaN_2O_{12}S_2Ni$ (**[Ni,Ca]**): C 37.29, H 3.37, N 3.34;

Found: C 37.55, H 3.59, N 3.15. Cyclic Voltammetry (0.1 M $[nBu_4N]^+[PF_6]^-$ in CH_3CN): $E_{1/2}$ = –1.682 V vs. $Fc^{+/0}$. Electronic absorption spectrum in CH_3CN (M^{-1} cm^{-1}): 388 (5940), 539 (129) nm.

[Ni,La]. Yield: 98%. ^1H NMR (500 MHz, CD_3CN) δ (ppm): 8.23 (s, 1H, *H3*), 8.16 (s, 1H, *H3*), 7.26 (d, $^3J_{H,H}$ =8.00, 1H, *H4*), 7.21 (d, $^3J_{H,H}$ =8.00, 1H, *H6*), 7.18 (d, $^3J_{H,H}$ =7.90, 2H, *H4*), 6.92 (t, $^3J_{H,H}$ =7.30, 1H, *H5*), 6.91 (t, $^3J_{H,H}$ =7.30, 1H, *H5*), 4.48 (m, 4H, *H7*), 4.21 (m, 4H, *H8*), 4.13 (s, 4H, *H9*), 3.42 (s, 2H, *H2*), 1.54 (s, 6H, *H1*). ^{13}C {^1H} NMR (126 MHz, CD_3CN) δ (ppm): 165.88, 162.36, 149.42, 149.32, 148.60, 147.96, 128.65, 128.14, 121.19, 121.00, 119.61, 119.59, 117.24, 72.23, 72.22, 70.61, 70.55, 69.59, 68.34, 25.33. ^{19}F NMR (471 MHz, CD_3CN) δ –79.94. Anal. Calcd. for $C_{27}H_{28}F_9LaN_2O_{15}S_3Ni$ (**[Ni,La]**): C 29.88, H 2.60, N 2.58; Found: C 29.63, H 2.85, N 2.50. Cyclic Voltammetry (0.1 M $[nBu_4N]^+[PF_6]^-$ in CH_3CN): $E_{1/2}$ = –1.423 V vs. $Fc^{+/0}$. Electronic absorption spectrum in CH_3CN (M^{-1} cm^{-1}): 370 (4576), 535 (87) nm.

[Ni,Y]. Yield: 97%. ^1H NMR (500 MHz, CD_3CN) δ (ppm): 7.85 (s, 1H, *H3*), 7.83 (s, 1H, *H3*), 7.28 (d, $^3J_{H,H}$ =8.00, 1H, *H4*), 7.20 (m, 1H, H6, *H4*), 6.95 (t, $^3J_{H,H}$ =8.00, 1H, *H5*), 6.92 (t, $^3J_{H,H}$ =8.00, 1H, *H5*), 4.51 (m, 4H, *H7*), 4.32 (m, 4H, *H8*), 4.22 (m, 4H, *H9*), 3.37 (s, 2H, *H2*), 1.55 (s, 6H, *H1*). ^{13}C {^1H} NMR (126 MHz, CD_3CN) δ (ppm): 165.39, 162.21, 147.98, 147.81, 147.73, 147.04, 128.25, 127.86, 121.34, 121.01, 120.04, 119.80, 117.21, 117.13, 71.83, 71.56, 71.24, 71.08, 70.42, 68.95, 68.70, 68.53, 25.24. ^{19}F NMR (376 MHz, CD_3CN) δ –80.06. Anal. Calcd. for $C_{27}H_{28}F_9N_2YO_{15}S_3Ni$ (**[Ni,Y]**): C 31.32, H 2.73, N 2.70; Found: C 29.08, H 2.91, N 2.61. Calcd. for $C_{27}H_{28}F_9N_2YO_{15}S_3Ni + CH_2Cl_2$: C 28.95, H 2.70, N 2.50. CH_2Cl_2 inclusion in the sample is likely due to the purification process of **[Ni,Y]**, which provided a crystalline powder with the same process used for the crystallization of **[Ni,La]** and **[Ni,Lu]**. Cyclic Voltammetry

(0.1 M $[nBu_4N]^+[PF_6]^-$ in CH_3CN): $E_{1/2}$ = –1.445 V vs. $Fc^{+/0}$. Electronic absorption spectrum in CH_3CN (M^{-1} cm^{-1}): 378 (4275), 532 (118) nm.

[Ni,Lu]. Yield: 97%. ^1H NMR (500 MHz, CD_3CN) δ (ppm): 7.90 (s, 1H, *H3*), 7.88 (s, 1H, *H3*), 7.28 (d, $^3J_{H,H}$ =8.05, 1H, *H4*), 7.21 (m, $^3J_{H,H}$ =8.05, 2H, *H6*), 7.20 (d, $^3J_{H,H}$ =8.00, 1H, *H4*), 6.95 (t, $^3J_{H,H}$ =8.00, 1H, *H5*), 6.93 (t, $^3J_{H,H}$ =8.05, 1H, *H5*), 4.51 (m, 4H, *H7*), 4.31 (m, 4H, *H8*), 4.22 (s, 4H, *H9*), 3.40 (s, 2H, *H2*), 1.55 (s, 6H, *H1*). ^{13}C {^1H} NMR (126 MHz, CD_3CN) δ (ppm): 165.27, 162.16, 147.97, 147.82, 147.80, 147.14, 128.31, 127.92, 121.61, 121.29, 120.10, 119.89, 117.55, 117.45, 71.69, 71.53, 71.45, 71.40, 70.39, 68.95, 68.79, 68.57, 25.27. ^{19}F NMR (376 MHz, CD_3CN) δ –80.05. Anal. Calcd. for $C_{27}H_{28}F_9N_2LuO_{15}S_3Ni$ (**[Ni,Lu]**): C 28.92, H 2.52, N 2.50; Found: C 27.87, H 2.84, N 2.83. Calcd. for $C_{27}H_{28}F_9N_2LuO_{15}S_3Ni$ + CH_2Cl_2 +0.25 CH_3CN: C 28.14, H 2.59, N 2.55. CH_2Cl_2 and CH_3CN are likely included in the sample due to the crystallization method used to purify **[Ni,Lu]**. Cyclic Voltammetry (0.1 M $[nBu_4N]^+[PF_6]^-$ in CH_3CN): $E_{1/2}$ = –1.426 V vs. $Fc^{+/0}$. Electronic absorption spectrum in CH_3CN (M^{-1} cm^{-1}): 374 (4369), 532 (113) nm.

ASSOCIATED CONTENT

Supporting Information. The following files are available free of charge.

NMR spectra; characterization data for the complexes reported in this work; electrochemical data and related analysis; and detailed information regarding the X-ray diffraction analysis (PDF)

Cartesian coordinates for the XRD structures (XYZ)

AUTHOR INFORMATION

Corresponding Author

E-mail: blakemore@ku.edu. Phone: (785) 864-3019

Author Contributions

The manuscript was written through contributions of all authors. All authors have given approval to the final version of the manuscript.

ACKNOWLEDGMENT

This work was supported by the U.S. Department of Energy, Office of Science, Office of Basic Energy Sciences through the Early Career Research Program (DE-SC0019169). J.P.K. was supported by a U.S. National Science Foundation Research Traineeship (NRT) at the University of Kansas (DGE-1922649).

REFERENCES

[1] Ramirez, B. L.; Lu, C. C. Rare-Earth Supported Nickel Catalysts for Alkyne Semihydrogenation: Chemo- and Regioselectivity Impacted by the Lewis Acidity and Size of the Support. *J. Am. Chem. Soc.* **2020**, *142*, 5396-5407.

[2] Tran, T. V.; Karas, L. J.; Wu, J. I.; Do, L. H. Elucidating Secondary Metal Cation Effects on Nickel Olefin Polymerization Catalysts. *ACS Catal.* **2020**, *10*, 10760-10772.

[3] Kanady, J. S.; Tsui, E. Y.; Day, M. W.; Agapie, T. Synthetic Model of the Mn_3Ca Subsite of the Oxygen-Evolving Complex in Photosystem II. *Science* **2011**, *333*, 733-736.

[4] Devi, T.; Lee, Y.-M.; Nam, W.; Fukuzumi, S. Tuning Electron-Transfer Reactivity of a Chromium(III)–Superoxo Complex Enabled by Calcium Ion and Other Redox-Inactive Metal Ions. *J. Am. Chem. Soc.* **2020**, *142*, 365-372.

[5] Kumar, A.; Lionetti, D.; Day, V.W.; Blakemore, J. D. Trivalent Lewis Acidic Cations Govern the Electronic Properties and Stability of Heterobimetallic Complexes of Nickel. *Chem. Eur. J.* **2018**, *24*, 141-149.

[6] Windorff, C. J.; Chen, G. P.; Cross, J. N.; Evans, W. J.; Furche, F.; Gaunt, A. J.; Janicke, M. T.; Kozimor, S. A.; Scott, B. L. Identification of the Formal +2 Oxidation State of Plutonium: Synthesis and Characterization of $\{Pu^{II}[C_5H_3(SiMe_3)_2]_3\}^-$. *J. Am. Chem. Soc.* **2017,** *139*, 3970-3973.

[7] Ryan, A. J.; Ziller, J. W.; Evans, W. J. The importance of the counter-cation in reductive rare-earth metal chemistry: 18-crown-6 instead of 2,2,2-cryptand allows isolation of $[Y^{II}(NR_2)_3]^{1-}$ and ynediolate and enediolate complexes from CO reactions. *Chem. Sci.* **2020,** *11*, 2006-2014.

[8] Kumar, A.; Lionetti, D.; Day, V.W.; Blakemore, J. D. Redox-Inactive Metal Cations Modulate the Reduction Potential of the Uranyl Ion in Macrocyclic Complexes. *J. Am. Chem. Soc.* **2020**, *142*, 3032-3041.

[9] Golwankar, R. R.; Kumar, A.; Day, V. W.; Blakemore, J. D. Revealing the Influence of Diverse Secondary Metal Cations on Redox-Active Palladium Complexes. *Chem. Eur. J.* **2022**, *28*, e202200344.

[10] Dopp, C. M.; Golwankar, R. R.; Kelsey, S. R.; Douglas, J. T.; Erickson, A. N.; Oliver, A. G.; Day, C. S.; Day, V. W.; Blakemore, J. D. Vanadyl as a Spectroscopic Probe of Tunable Ligand Donor Strength in Bimetallic Complexes. *Inorg. Chem.* **2023**, *62*, 9827-9843.

[11] Langley, S. K.; Le, C.; Ungur, L.; Moubaraki, B.; Abrahams, B. F.; Chibotaru, L. F.; Murray, K. S. Heterometallic 3d–4f Single-Molecule Magnets: Ligand and Metal Ion Influences on the Magnetic Relaxation. *Inorg. Chem.* **2015,** *54*, 3631-3642.

[12] Reath, A. H.; Ziller, J. W.; Tsay, C.; Ryan, A. J.; Yang, J. Y. Redox Potential and Electronic Structure Effects of Proximal Nonredox Active Cations in Cobalt Schiff Base Complexes. *Inorg. Chem.* **2017**, *56*, 3713-3718.

[13] Kang, K.; Fuller, J.; Reath, A. H.; Ziller, J. W.; Alexandrova, A. N.; Yang, J. Y. Installation of internal electric fields by non-redox active cations in transition metal complexes. *Chem. Sci.* **2019**, *10*, 10135-10142.

[14] Truter, M. R., Alkali Metal Complexes with Organic Ligands, *Structure and Bonding,* **1973**, *16*, 71-111

[15] Perrin, D. D. *Ionisation Constants of Inorganic Acids and Bases in Aqueous Solution*; Pergamon Press: New York, 1982.

[16] Kumar, A.; Blakemore, J. D. On the Use of Aqueous Metal-Aqua pKa Values as a Descriptor of Lewis Acidity. *Inorg. Chem.* **2021**, *60*, 1107-1115.

[17] Golwankar, R. R.; Curry II, T. D.; Paranjothi, C. J.; Blakemore, J. D. Molecular Influences on the Quantification of Lewis Acidity with Phosphine Oxide Probes. *Inorg. Chem*. **2023**, *62*, 9765-9780.

[18] Wulfsberg, G. *Principles of Descriptive Inorganic Chemistry*. University Science Books: Mill Valley, Calif., 1991, pp. 27-31.

[19] Shannon, R.D.; Prewitt, C.T. Revised values of effective ionic radii. *Acta Crystallogr.* **1970**, *B26*, 1046-1048.

[20] Shannon, R.D. Revised effective ionic radii and systematic studies of interatomic distances in halides and chalcogenides. *Acta Crystallogr.* **1976**, *A32*, 751-767.

[21] Van Staveren, C.J.; Van Eerden, J.; Van Veggel, F. C. J. M.; Harkema, S.; Reinhoudt, D. N. Cocomplexation of neutral guests and electrophilic metal cations in synthetic macrocyclic hosts. *J. Am. Chem. Soc.* **1988**, *110*, 4994-5008.

[22] Van Veggel, F. C. J. M.; Harkema, S.; Bos, M.; Verboom, W.; Van Staveren, C.J.; Gerritsma, G. J.; Reinhoudt, D. N. Metallomacrocycles: synthesis, x-ray structure, electrochemistry, and ESR spectroscopy of mononuclear and heterodinuclear complexes. *Inorg. Chem.* **1989**, *28*, 1133-1148.

[23] Beesley, R. M.; Ingold, C. K.; Thorpe, J.F. CXIX.−The formation and stability of spiro-compounds. Part I. spiro-Compounds from cyclohexane. *J. Chem. Soc. Trans.* **1915**, *107*, 1080-1106.

[24] Groom, C. R.; Bruno, I. J.; Lightfoot, M. P.; Ward, S. C., The Cambridge Structural Database. *Acta Cryst. B* **2016,** *72*, 171-179.

[25] (a) Bag, B.; Mondal, N.; Rosair, G.; Mitra, S. CCDC 151498: Experimental Crystal Structure Determination, **2001**, DOI: 10.5517/cc52n1x. (b) Bag, B.; Mondal, N.; Rosair, G.; Mitra, S. The First Thermally-stable Singly Oxo-bridged Dinuclear Ni(III) Complex. *Chem. Commun.* **2000,** 1729-1730.

[26] (a) Zhou, H.; Pan, Z.-Q.; Zhang, Y.-J. CCDC 625054: Experimental Crystal Structure Determination, **2006**, DOI: 10.5517/ccnzf12. (b) Zhou, H.; Pan, Z.-Q.; Zhang, Y.-J. Acetato[μ -10,21-dibutyl-3,6,14,17-tetrazatricyclo[17.3.1.18,12]tetracosa-1(23),2,6,8,10,12(24),13,17,19,21-decaene-23,24-diolato(2- κ4N_3,N6,O23,O24: κ 4N14,N17,O23,O24]dinickel(II) perchlorate acetonitrile hemisolvate. *Acta Cryst. E* **2006,** *62*, m2442-m2444.

[27] (a) Wu, J.-C.; Li, Y.-Z.; Tang, N.; Tan, M.-Y. CCDC 217382: Experimental Crystal Structure Determination, **2003**, DOI: 10.5517/cc796b1. (b) Wu, J.-C.; Li, Y.-Z.; Tang, N.; Tan, M.-Y. [μ -10,21-Di-tert-butyl-4(*S*),5(*S*),15(*S*),16(*S*)-tetraphenyl-3,6,14,17-tetraazatricyclo[17.3.1.18,12]tetracosa-1(23),2,6,8,10,12(24),13,17,19,21-decaene-23,24-diolato](μ -ethylene glycol)dinickel(II) diperchlorate dihydrate. *Acta Cryst. E* **2003,** *59*, m494-m496.

[28] (a) Ding, Y.; Ku, Z.; Wang, L.; Hu, Y.; Zhou, Y. CCDC 654305: Experimental Crystal Structure Determination, **2008**, DOI: 10.5517/ccpyvm2. (b) Ding, Y.; Ku, Z.; Wang, L.; Hu, Y.; Zhou, Y. Bis{μ-2,2'-[ethane-1,2-diylbis(nitrilomethylidyne)]diphenolato}dinickel(II). *Acta Cryst. E* **2008,** *64*, m173. (c) Ding, Y.; Wang, F.; Ku, Z. J.; Wang, L. S.; Wang, Q. R. Solvent directed templated synthesis of mono- and di(Schiff base) complexes of Ni(II). *Russ. J. Coord. Chem.* **2009,** *35*, 360-366..

[29] (a) Tang, C. CCDC 722825: Experimental Crystal Structure Determination, **2009**, doi: 10.5517/ccs84y3. (b) Wu, Q.; Tang, Y.-F.; Zi, Q.-L. CCDC 1892682: Experimental Crystal Structure Determination, **2019**, doi: 10.5517/ccdc.csd.cc21jh8c.

[30] Yang, L.; Powell, D. R.; Houser, R. P. Structural variation in copper(I) complexes with pyridylmethylamide ligands: structural analysis with a new four-coordinate geometry index, τ4. *Dalton Trans.*, **2007**, 955-964.

[31] Lever, A.B.P. *Inorganic Electronic Spectroscopy*, 2nd ed.; Elsevier Science Publishers, 1984

[32] Selbin, J. Oxovanadium(IV) complexes. *Coord. Chem. Rev.* **1966,** *1*, 293-314.

[33] Kelsey, S.R.; Kumar, A.; Oliver, A.G.; Day, V.W.; Blakemore, J. D. Promotion and Tuning of the Electrochemical Reduction of Hetero- and Homobimetallic Zinc Complexes. *ChemElectroChem* **2021**, *8*, 2792-2751.

[34] Isse, A.A.; Gennaro, A.; Vianello, E. A study of the electrochemical reduction mechanism of Ni(salophen) in DMF. *Electrochim Acta.* **1992**, *37*, 113-118.

[35] (a) Gosden, C.; Healy, K. P.; Pletcher, D. Reaction of electrogenerated square-planar nickel(I) complexes with alkyl halides. *J. Chem. Soc., Dalton Trans.* **1978**, 972-976. (b) Duñach, E.; Esteves, A. P.; Medeiros, M. J.; Pletcher, D.; Olivero, S. The Study of Nickel(II) and Cobalt(II) Complexes with a Chiral Salen Derivative as Catalysts for the Electrochemical Cyclisation of Unsaturated 2-bromophenyl Ethers. *J. Electroanal. Chem.* **2004,** *566*, 39-45.

[36] Dopp, C. M. Using Vanadyl and Its Terminal Oxo to Probe Ligand Donor Strength in Heterobimetallic Complexes, Undergraduate Thesis, University of Kansas, **2023**, http://hdl.handle.net/1808/34384

[37] Bard, A. J.; Faulkner, L. R. *Electrochemical Methods: Fundamentals and Applications*; John Wiley and Sons, Inc., 1980.

[38] Hopkins Leseberg, J.A., Gompa, T.P., Oliver, A.G., Day, V.W., La Pierre, H.S., and Blakemore, J.D., Rational Tuning of Cerium Redox Chemistry with Mono- and Divalent Redox-Inactive Metal Cations, **2023**, *submitted*.

[39] Savéant, J.-M.; Costentin, C. *Elements of Molecular and Biomolecular Electrochemistry*, 2nd ed.; Wiley, 2019.

[40] Connelly, N. G.; Geiger, W. E. Chemical Redox Agents for Organometallic Chemistry. *Chem. Rev.* **1996**, *96*, 877-910.

[41] (a) Miedaner, A.; Haltiwanger, R. C.; DuBois, D. L. Relationship between the bite size of diphosphine ligands and tetrahedral distortions of "square-planar" nickel(II) complexes: stabilization of nickel(I) and palladium(I) complexes using diphosphine ligands with large bites. *Inorg. Chem.* **1991**, *30*, 417-427. (b) Gomes, L.; Pereira, E.; Castro, B. Nickel(II) complexes with N2OS and N2S2 co-ordination spheres: reduction and spectroscopic study of the corresponding Ni(I) complexes. *J. Chem. Soc., Dalton Trans.* **2000**, 1373-1379.

[42] Stoll, S.; Schweiger, A. EasySpin, a comprehensive software package for spectral simulation and analysis in EPR. *J. Magn. Reason.* **2006**, *178*, 42-55.

[43] Nicholson, R. S. Theory and Application of Cyclic Voltammetry for Measurement of Electrode Reaction Kinetics. *Anal. Chem.* **1965**, *37*, 1351-1355.

[44] Brunschwig, B. S.; Creutz, C.; Macartney, D. H.; Sham, T. K.; Sutin, N. The Role of Inner-sphere Configuration Changes in Electron-exchange Reactions of Metal Complexes. *Faraday Discuss. Chem. Soc.* **1982,** *74*, 113-127.

[45] Marcus, R. A.; Sutin, N. Electron transfers in chemistry and biology. *Biochim. Biophys. Acta – Rev. Bioenerg.* **1985,** *811*, 265-322.

[46] Brunschwig, B. S.; Logan, J.; Newton, M. D.; Sutin, N. A Semiclassical Treatment of Electron-exchange Reactions. Application to the Hexaaquoiron(II)-hexaaquoiron(III) System. *J. Am. Chem. Soc.* **1980,** *102*, 5798-5809.

[47] Bangle, R. E.; Schneider, J.; Piechota, E. J.; Troian-Gautier, L.; Meyer, G. J. Electron Transfer Reorganization Energies in the Electrode–Electrolyte Double Layer. *J. Am. Chem. Soc.* **2020,** *142*, 674-679.

[48] (a) Hush, N. S. Adiabatic theory of outer sphere electron-transfer reactions in solution. *Trans. Faraday Soc.* **1961**, *57*, 557-580. (b) Marcus, R. A. On the Theory of

Oxidation-Reduction Reactions Involving Electron Transfer. I. *J. Chem. Phys.* **2004**, *24*, 966-978. (c) Marcus, R. A. On the Theory of Electron-Transfer Reactions. VI. Unified Treatment for Homogeneous and Electrode Reactions. *J. Chem. Phys.* **2004**, *43*, 679-701. (d) Sutin, N. Nuclear, electronic, and frequency factors in electron transfer reactions. *Acc. Chem. Res.* **1982**, *15*, 275-282. (e) Liu, Y.-P.; Newton, M. D. Reorganization Energy for Electron Transfer at Film-Modified Electrode Surfaces: A Dielectric Continuum Model. *J. Phys. Chem.* **1994**, *98*, 7162-7169. (f) Ghosh, S.; Horvath, S.; Soudackov, A. V.; Hammes-Schiffer, S. Electrochemical Solvent Reorganization Energies in the Framework of the Polarizable Continuum Model. *J. Chem. Theory Comp.* **2014**, *10*, 2091-2102. (g) Spitler, M. T. Effect of nanometer-sized surface morphology upon electrochemical kinetics. *Electrochim. Acta* **2007**, *52*, 2294-2301.

[49] Amashukeli, X.; Winkler, J. R.; Gray, H. B.; Gruhn, N. E.; Lichtenberger, D. L. Electron-Transfer Reorganization Energies of Isolated Organic Molecules. *J. Phys. Chem. A* **2002,** *106*, 7593-7598.

[50] Wenger, O. S.; Leigh, B. S.; Villahermosa, R. M.; Gray, H. B.; Winkler, J. R. Electron Tunneling Through Organic Molecules in Frozen Glasses. *Science* **2005,** *307*, 99-102.

[51] Closs, G. L.; Miller, J. R. Intramolecular Long-Distance Electron Transfer in Organic Molecules. *Science* **1988,** *240*, 440-447.

[52] Creutz, C.; Sutin, N. Vestiges of the "Inverted Region" for Highly Exergonic Electron-transfer Reactions. *J. Am. Chem. Soc.* **1977,** *99*, 241-243.

[53] Falivene, L.; Credendino, R.; Poater, A.; Petta, A.; Serra, L.; Oliva, R.; Scarano, V.; Cavallo, L. SambVca 2. A Web Tool for Analyzing Catalytic Pockets with Topographic Steric Maps. *Organometallics* **2016,** *35*, 2286-2293.

[54] (a) Poater, A.; Ragone, F.; Giudice, S.; Costabile, C.; Dorta, R.; Nolan, S. P.; Cavallo, L. Thermodynamics of N-Heterocyclic Carbene Dimerization: The Balance of Sterics and Electronics. *Organometallics* **2008**, *27*, 2679-2681. (b) Poater, A.; Ragone, F.; Mariz, R.; Dorta, R. Cavallo, L. Comparing the Enantioselective Power of Steric and Electrostatic Effects in Transition-Metal-Catalyzed Asymmetric Synthesis. *Chem. Eur. J. Int Ed.* **2010**, *16*, 14348-14353. (c) Falivene, L.; Cao, Z.; Petta, A.; Serra, L.; Poater, A.; Oliva, R.; Scarano, V.; Cavallo, L. Towards the online computer-aided design of catalytic pockets. *Nat. Chem.* **2019**, *11*, 872-879.

[55] Wüthrich, K. E.S.R. (Electron Spin Resonance) Investigation of VO^{2+} Complex Compounds in Aqueous Solution. II. *Helv. Chim. Acta* **1965,** *48*, 1012-1017.

[56] (a) Chasteen, N. D., "Vanadyl(IV) EPR spin probes. Inorganic and Biochemical Aspects," in *Biol. Magn. Reson.*; Berliner, L. J., Reuben, J., Ed.; Plenum Press: New York, 1981; Chapter 2, Vol. 3, pp. 53-119. (b) Dickson, F. E.; Petrakis, L. Application of electron spin resonance and electronic spectroscopy to the characterization of vanadium species in petroleum fractions. *Anal. Chem.* **1974,** *46*, 1129-1130. (c) Smith, T. S.; LoBrutto, R.; Pecoraro, V. L. Paramagnetic spectroscopy of vanadyl complexes and its applications to biological systems. *Coord. Chem. Rev.* **2002,** *228*, 1-18.

[57] (a) Holyk, N. H. An Electron Paramagnetic Resonance Study of Model Oxovanadium(IV) Complexes in Aqueous Solution: Correlation of Magnetic Properties with Ligand Type and

Metal Chelate Structure. M.S. Thesis, University of New Hampshire, Durham, NH, 1979. (b) Mannikko, D.; Stoll, S. Vanadyl Porphyrin Speciation Based on Submegahertz Ligand Proton Hyperfine Couplings. *Energy Fuels* **2019,** *33*, 4237-4243.

[58] Xiong, S.; Hong, A.; Bailey, B. C.; Spinney, H. A.; Senecal, T. D.; Bailey, H.; Agapie, T. Highly Active and Thermally Robust Nickel Enolate Catalysts for the Synthesis of Ethylene-Acrylate Copolymers. *Angew. Chem. Int. Ed.* **2022**, *61*, e202206637.

[59] Wu, K.; Doyle, A. G. Parameterization of phosphine ligands demonstrates enhancement of nickel catalysis via remote steric effects. *Nat. Chem.* **2017**, *9*, 779-784.

[60] Fukuzumi, S.; Ohkubo, K.; Lee, Y.-M.; Nam, W. Lewis Acid Coupled Electron Transfer of Metal–Oxygen Intermediates. *Chem. Eur. J.* **2015,** *21*, 17548-17559.

[61] (a) Oswald, V. F.; Lee, J. L.; Biswas, S.; Weitz, A. C.; Mittra, K.; Fan, R.; Li, J.; Zhao, J.; Hu, M. Y.; Alp, E. E.; et al. Effects of Noncovalent Interactions on High-Spin Fe(IV)–Oxido Complexes. *J. Am. Chem. Soc.* **2020**, *142*, 11804-11817. (b) Prat, J. R.; Gaggioli, C. A.; Cammarota, R. C.; Bill, E.; Gagliardi, L.; Lu, C. C. Bioinspired Nickel Complexes Supported by an Iron Metalloligand. *Inorg. Chem.* **2020**, *59*, 14251-14262.

[62] (a) Krivovichev, S. V.; Cahill, C. L.; Burns, P. C. Syntheses and Crystal Structures of Two Topologically Related Modifications of $Cs_2[(UO_2)_2(MoO_4)_3]$. *Inorg. Chem.* **2002,** *41*, 34-39. (b) Frisch, M.; Cahill, C. L. Syntheses, structures and fluorescent properties of two novel coordination polymers in the U-Cu-H_3pdc system. *Dalton Trans* **2005,** 1518-1523. (c) Cahill, C. L.; de Lill, D. T.; Frisch, M. Homo- and heterometallic coordination polymers from the f elements. *CrystEngComm* **2007,** *9*, 15-26.

[63] Arnold, P. L.; Patel, D.; Wilson, C.; Love, J. B. Reduction and selective oxo group silylation of the uranyl dication. *Nature* **2008,** 451, 315-317.

TOC Graphic

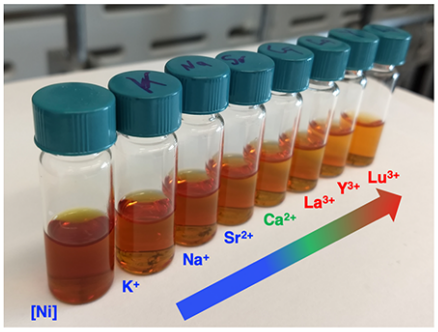

- *Ionic radius as a descriptor for structural features in crown ether complexes*
- *Free volume as a descriptor for electron transfer rates for NiII/NiI redox*
- *EPR studies of tunable nickel(I) species*

Mapping Steric Crowding in the Nickel Microenvironment

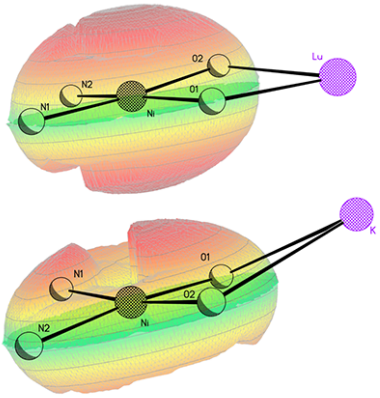

TOC Synopsis

The synthesis and redox properties of heterobimetallic nickel complexes supported by a tailored ditopic ligand have been investigated. The complexes incorporate a range of secondary mono-, di-, and trivalent metal cations in the form of their triflate salts. Spectroscopic data (EPR) show that the first site of reduction is nickel-centered while electrochemical studies show that the identity of the secondary metal cation influences the rate of electron transfer to the nickel center. A free volume analysis demonstrates that crowding of the triflate counteranions into the microenvironment about the nickel site results in the modulated electron transfer rates.